PHYSICAL REVIEW D **84,** 044057 (2011)

Characteristic extraction tool for gravitational waveforms

M. C. Babiuc,[1,3] B. Szilágyi,[2,3] J. Winicour,[3,4] and Y. Zlochower[5]

[1]*Department of Physics, Marshall University, Huntington, West Virginia 25755, USA*
[2]*Theoretical Astrophysics, California Institute of Technology, Pasadena, California 91125, USA*
[3]*Department of Physics and Astronomy, University of Pittsburgh, Pittsburgh, Pennsylvania 15260, USA*
[4]*Max-Planck-Institut für Gravitationsphysik, Albert-Einstein-Institut, 14476 Golm, Germany*
[5]*Center for Computational Relativity and Gravitation and School of Mathematical Sciences, Rochester Institute of Technology, Rochester, New York 14623, USA*

(Received 17 November 2010; published 29 August 2011)

We develop and calibrate a characteristic waveform extraction tool whose major improvements and corrections of prior versions allow satisfaction of the accuracy standards required for advanced LIGO data analysis. The extraction tool uses a characteristic evolution code to propagate numerical data on an inner worldtube supplied by a $3 + 1$ Cauchy evolution to obtain the gravitational waveform at null infinity. With the new extraction tool, high accuracy and convergence of the numerical error can be demonstrated for an inspiral and merger of mass M binary black holes even for an extraction worldtube radius as small as $R = 20M$. The tool provides a means for unambiguous comparison between waveforms generated by evolution codes based upon different formulations of the Einstein equations and based upon different numerical approximations.

DOI: 10.1103/PhysRevD.84.044057 PACS numbers: 04.20.Ex, 04.25.Nx, 04.30.Db, 04.70.Bw

I. INTRODUCTION

The strong emission of gravitational waves from the inspiral and merger of binary black holes has been a dominant motivation for the construction of gravitational wave observatories. The computation of the precise details of the waveform by means of numerical simulation is a key theoretical tool to enhance detection and allow useful scientific interpretation of the gravitational signal. See [1] for a review of the accuracy required of numerically generated waveforms to fully complement the sensitivity of the LIGO [2] and Virgo [3] observatories. However, the waveforms are not easy to extract accurately. The radiation falls off as $1/r$ so that although it asymptotically dominates near field gravitational effects it is nevertheless small and can be contaminated by numerical error. It is common practice for the Cauchy codes used in simulating the binary black hole problem to introduce a large but finite artificial outer boundary. A combination of linearized and far field approximations are then used to extract the waveform from data on a smaller worldtube, which ideally is causally isolated from the outer boundary. Such perturbative wave extraction at a finite distance, rather than at null infinity which more faithfully represents the idealization of a distant antenna, introduces systematic errors associated with the effects of gauge, nonlinearities, nonradiative near fields and back reflection. (See [4,5] for analyses of waveform errors arising from perturbative extraction at a finite distance.) An alternative approach called *Cauchy-characteristic extraction* (CCE) [6,7] provides a fully nonlinear interface between Cauchy and characteristic codes which utilizes the characteristic evolution to extend the simulation to null infinity, where the waveform is computed. An earlier implementation of CCE has recently been applied to extract waveforms from binary black hole simulations [8,9], from rotating stellar core collapse [10] and to explore the memory effect [11]. In this work, we present details and tests of a redesigned CCE module whose accuracy and efficiency has undergone major improvement. The module has been designed to provide a standardized waveform extraction tool for the numerical relativity community which will allow CCE to be readily applied to a generic Cauchy code.

The first attempts to simulate collisions of black holes by Hahn and Lindquist [12], and then by Smarr *et al.* [13], were hampered by both a lack of computing power and a proper understanding of the mathematical formulation of Einstein's equations required for a stable numerical solution. Their work formed the impetus for the Binary Black Hole Grand Challenge, which was formed to take advantage of the increasingly powerful computers introduced in the 1980s. The main results of the Grand Challenge were limited to the axisymmetric head-on collision of black holes and the gravitational collapse of rotating matter [14]. However, the standard Arnowitt-Deser-Misner [15] formulation of the Einstein equations adopted by the Grand Challenge had instabilities at the analytic level which limited more general binary black hole simulations to the premerger stage. Only with new formulations was a full inspiral and merger successful, first by Pretorius [16] using the harmonic formulation, and soon after by Campanelli *et al.* [17] and Baker *et al.* [18] using the Baumgarte-Shapiro-Shibabta-Nakamura formulation [19,20]. Numerous groups now have codes which can simulate this binary inspiral problem by evolving the Cauchy problem for Einstein's equations.

In CCE, the Cauchy evolution is used to supply boundary data on a timelike inner worldtube to carry out a characteristic evolution extending to future null infinity $\mathcal{I}^+$, where the waveform can be unambiguously computed using the geometric methods developed by Bondi *et al.* [21], Sachs [22] and Penrose [23]. This initial-boundary value problem based upon a timelike worldtube [24] has been implemented as a characteristic evolution code, the PITT null code [25,26], which incorporates a Penrose compactification of the space-time. It computes the Bondi news function at $\mathcal{I}^+$, which is an invariantly defined complex radiation amplitude $N = N_\oplus + iN_\otimes$, whose real and imaginary parts correspond to the time derivatives $\partial_t h_\oplus$ and $\partial_t h_\otimes$ of the "plus" and "cross" polarization modes of the strain incident on a gravitational wave antenna. The error in the PITT code was tested to be second order convergent in analytic testbeds ranging from the perturbative regime [27] to highly nonlinear single black hole spacetimes [26]. One of the successes of the Grand Challenge was the successful application of the code to generic single black hole dynamical spacetimes [28–31]. For a review, see [32].

The propagation of gravitational waves to $\mathcal{I}^+$ from an astrophysically realistic source using the PITT code has in the past been limited to the simulation of an imploding neutron star using a fluid dynamic code incorporated into the characteristic code [33,34]. These simulations were restricted to the axisymmetric case because of computational demands arising at the center of the star. For such systems, CCE offers a way to combine the strengths of the Cauchy and characteristic approaches. Recently this combined approach has been applied to extract the waveform from the fully 3-dimensional collapse of a rotating star [10]. A global characteristic simulation of the full inspiral and merger of a relativistic binary system is not possible because of the interior caustics formed by gravitational lensing. But the application of CCE to this system has been shown to be possible [8,9].

The error in CCE arises from three independent sources: *(I)* the Cauchy evolution; *(II)* the worldtube module; and *(III)* the characteristic evolution to $\mathcal{I}^+$ and the computation of the waveform.

(i) Errors in the Cauchy evolution can arise from numerical approximations, improper boundary treatments, extraneous radiation content in the initial data, instabilities and bugs. Errors introduced at the outer grid boundary present a special problem for BSSN formulations for which there is no theoretical understanding of the proper boundary condition. The standard practice is to extract the waveform at a finite worldtube which is large enough to justify a far field approximation but which is causally isolated from the outer boundary during the simulation. For example, perturbative extraction at $r = 100M$ would require that the outer boundary be at $r > 500M$ for a $t \approx 400M$ simulation. We have designed the new CCE module so that it can be applied to a generic Cauchy code with extraction radius as small as $r = 20M$. However, since any universally applicable extraction module must be designed to be independent of error introduced by the Cauchy code, the extracted waveform cannot be any more reliable than the Cauchy code.

(ii) The main improvement described and tested in this paper is a complete overhaul of the worldtube module, which converts the output of the Cauchy evolution to boundary data on an inner worldtube for the characteristic evolution. The prior version of this module, which was used in the first applications of CCE to obtain binary black hole waveforms [8–10], contained inconsistencies and bugs which prevented clean convergence tests. We have corrected this worldtube module so that the present version exhibits clean convergence to which Richardson extrapolation can be applied to produce waveforms whose numerical error due to CCE is extremely small. In addition to improvement in consistency and accuracy, we have also redesigned the module to be more efficient and user friendly. These revisions are described in the Appendix.

(iii) In addition to thoroughly scrutinizing the PITT null code for bugs, we made several major modifications. In previous applications requiring very high resolution, such as the inspiral of a particle into a black hole [35], there was excessive short wavelength noise which affected the quality of the simulation. In addition, in [8,9] it was reported that one of the equations governing calculation of the waveform at $\mathcal{I}^+$ had to be linearized in order to obtain reasonable behavior. These problems have been eliminated as a result of the modifications described in the Appendix.

In Secs. II and III, we review the formalism underlying characteristic evolution and the computational structure of the PITT code. We include enough details to make clear the difficulties underlying extraction of an accurate waveform at $\mathcal{I}^+$ and to explain the code modifications that have been made. We also demonstrate how the use of 4th order accurate angular derivatives improves the previous test results of CCE presented in [5]. In Sec. IV, we describe the design of the new worldtube module, how it treats the Cauchy-characteristic interface and how it can be readily applied to a Cauchy evolution.

In Sec. V, we test the new extraction tool on the Cauchy evolution of the inspiral and merger of two equal-mass, nonspinning black holes. We show that CCE can now be carried out for a worldtube radius as small as $20M$ for a mass M binary system, for which perturbative extraction would not be meaningful, and which was not possible with the prior implementation of CCE. Convergence tests now

demonstrate clean second order global accuracy of the evolution variables.

The waveforms are only first order accurate as a result of the asymptotic limits required at $\mathcal{I}^+$. However, the clean first order convergence of the waveform now allows application of Richardson extrapolation to obtain higher order accuracy. In this way, in Sec. VI, we construct a third order accurate waveform, which was not possible with earlier versions of CCE.

The ability to apply Richardson extrapolation to CCE waveforms makes it possible to show that their numerical error satisfies the standards required for application to advanced LIGO data analysis. The first derivation [36] of the accuracy required for numerically generated black hole waveforms to be useful as templates for LIGO was carried out in the frequency domain, in which the interferometer noise spectrum is calibrated. There are two separate criteria: one ensures that the error in the model waveform does not impact wave detection and the other ensures that the error does not impact the scientific content of the signal. These criteria both depend upon the noise spectrum of the detector in a way not easily applied to a numerical simulation. This has recently prompted a translation of these requirements into the time domain in which the waveforms are computed [1,37,38], so that they can be readily enforced in practice. In Sec. VII we show that the numerical error introduced by CCE satisfies these time domain criteria for an advanced LIGO detector. We also analyze the error introduced by the choice of initial data, which has a dependency upon the size of the extraction worldtube.

II. CHARACTERISTIC FORMALISM

The characteristic formalism is based upon a family of outgoing null hypersurfaces emanating from an inner worldtube and extending to infinity where they foliate $\mathcal{I}^+$ into spherical slices. We let u label these hypersurfaces, x^A ($A = 2, 3$) be angular coordinates which label the null rays and r be a surface-area coordinate. In the resulting $x^\alpha = (u, r, x^A)$ coordinates, the metric takes the Bondi-Sachs form [21,22]

$$ds^2 = -\left(e^{2\beta}\frac{V}{r} - r^2 h_{AB}U^A U^B\right)du^2 - 2e^{2\beta}dudr - 2r^2 h_{AB}U^B du dx^A + r^2 h_{AB}dx^A dx^B, \tag{2.1}$$

where $h^{AB}h_{BC} = \delta^A_C$ and $\det(h_{AB}) = \det(q_{AB})$, with q_{AB} a unit sphere metric. In analyzing the Einstein equations, we also use the intermediate variable

$$Q_A = r^2 e^{-2\beta} h_{AB} U^B_{,r}. \tag{2.2}$$

Because the Bondi variable $V = O(r^2)$ at $\mathcal{I}^+$, the code is written in terms or the renormalized variable $W = (V - r)/r^2$. Here $W = 0$ for the Minkowski metric in null spherical coordinates.

The PITT null code employs a spherical grid based upon an auxiliary unit sphere metric q_{AB}, with associated complex dyad q_A satisfying $q_{AB} = \frac{1}{2}(q_A \bar{q}_B + \bar{q}_A q_B)$. The Bondi-Sachs metric h_{AB} induced on the spherical cross-sections can then be represented by its dyad component $J = h_{AB}q^A q^B/2$, with the spherically symmetric case characterized by $J = 0$. The fully nonlinear h_{AB} is uniquely determined by J, which is the principle evolution variable. The determinant condition implies that the dyad component $K = h_{AB}q^A \bar{q}^B/2$ is determined by $1 = K^2 - J\bar{J}$. We also introduce spin-weighted fields $U = U^A q_A$ and $Q = Q_A q^A$, as well as the complex spin-weight operators $\eth$ and $\bar{\eth}$ [39] which represent the angular derivatives. Refer to [40] for details regarding numerical implementation.

In this formalism, the Einstein equations decompose into hypersurface equations, evolution equations and conservation conditions on the inner worldtube. As described in more detail in [7,24], the hypersurface equations take the form

$$\beta_{,r} = N_\beta[J], \tag{2.3}$$

$$(r^2 Q)_{,r} = -r^2(\bar{\eth}J + \eth K)_{,r} + 2r^4 \eth(r^{-2}\beta)_{,r} + N_Q[J, \beta], \tag{2.4}$$

$$U_{,r} = r^{-2}e^{2\beta}Q + N_U[J, \beta, Q], \tag{2.5}$$

$$V_{,r} = \frac{1}{2}e^{2\beta}\mathcal{R} - e^\beta \eth\bar{\eth}e^\beta + \frac{1}{4}r^{-2}(r^4(\eth\bar{U} + \bar{\eth}U))_{,r} + N_W[J, \beta, Q, U], \tag{2.6}$$

where

$$\mathcal{R} = 2K - \eth\bar{\eth}K + \frac{1}{2}(\bar{\eth}^2 J + \eth^2 \bar{J}) + \frac{1}{4K}(\bar{\eth}\bar{J}\eth J - \bar{\eth}J\eth\bar{J}) \tag{2.7}$$

is the curvature scalar of the 2-metric h_{AB}. The evolution equation for J takes the form

$$2(rJ)_{,ur} - (r^{-1}V(rJ)_{,r})_{,r} = -r^{-1}(r^2\eth U)_{,r} + 2r^{-1}e^\beta \eth^2 e^\beta - (r^{-1}V)_{,r}J + N_J[J, J_{,u}, \beta, Q, U, W], \tag{2.8}$$

where $N_\beta[J]$, $N_Q[J, \beta]$, $N_U[J, \beta, Q]$, $N_W[J, \beta, Q, U]$ and $N_J[J, J_{,u}, \beta, Q, U, W]$ are nonlinear terms which vanish for spherical symmetry and can be constructed from the hypersurface values of the variables appearing in their argument. Expressions for these nonlinear terms as complex spin-weighted fields and a discussion of the conservation conditions are given in [7]. The hypersurface equations have a hierarchical structure in the order $[J, \beta, Q, U, W]$ such that the right hand sides, e.g. $N_\beta[J]$ only depend upon previous variables and their derivatives intrinsic to the hypersurface.

The finite-difference grid used in the code is based upon the compactified radial coordinate

$$x = \frac{r}{R_E + r} \tag{2.9}$$

so that $x = 1$ at $\mathcal{I}^+$. Here R_E is a parameter which in the CCE module is chosen as the radius of the extraction worldtube as determined by $R^2 = \delta_{ij}x^i x^j$ in terms of the Cartesian coordinates x^i used in the Cauchy evolution code.

The auxiliary variables

$$\nu = \bar{\eth} J, \qquad \mathcal{B} = \eth\beta, \qquad k = \eth K \tag{2.10}$$

are also introduced to eliminate all second angular derivatives. In certain applications this has been found to give rise to increased accuracy by suppressing short wavelength error [41].

The finite-difference scheme for integrating the hypersurface and evolution equations has been described in [26,41,42]. Except for the start-up procedure described in Sec. IV, we follow this scheme with two modifications. First, the finite-difference approximation for the $\eth$-operators is increased from 2nd order to 4th order accuracy. This can be expected to give better angular resolution but does not affect the overall 2nd order accuracy implied by the radial and time integration schemes. Second, when rewritten in terms of the compactified x-coordinate, the hypersurface equations for Q and W take the form

$$x(1 - x)\partial_x F + 2F = \text{RHS} \tag{2.11}$$

where the right hand side is regular at $\mathcal{I}^+$. In order to deal with the degeneracy of this equation at $x = 1$, we rewrite (2.11) in the form

$$\frac{\partial(r^2 F)}{\partial(r^2)} = \frac{\text{RHS}}{2} \tag{2.12}$$

and construct a centered finite-difference approximation with respect to r^2. Expressed in terms of the grid $x_i = x_{i-i} + \Delta x$, this leads to

$$F_i = \left(\frac{x_{i-1}(1 - x_i)}{x_i(1 - x_{i-1})}\right)^2 F_{i-1} + \frac{\Delta x(x_i + x_{i-1} - 2x_i x_{i-1})}{x_i^2(1 - x_{i-1})^2}\,\frac{\text{RHS}}{2} \tag{2.13}$$

which enforces the correct asymptotic limit $F|_{x=1} = \text{RHS}/2$ when RHS is constant near $\mathcal{I}^+$. In practice, the variation of RHS implies that this limit is only enforced to first order accuracy when RHS is evaluated by the midpoint rule. This is consistent with global second order accuracy of Q and W when the numerical error is measured by an L_2-norm over the hypersurface, but only first order accuracy can be expected for their values at $\mathcal{I}^+$. However, the asymptotic values of Q and W do not enter directly into the calculation of the waveform at $\mathcal{I}^+$.

A. Waveforms at $\mathcal{I}^+$

For technical simplicity, the theoretical derivation of the waveform at infinity is best presented in terms of an inverse surface-area coordinate $\ell = 1/r$, where $\ell = 0$ at $\mathcal{I}^+$. In the resulting $x^\mu = (u, \ell, x^A)$ conformal Bondi coordinates, the physical space-time metric $g_{\mu\nu}$ has the conformal compactification $\hat{g}_{\mu\nu} = \ell^2 g_{\mu\nu}$, where $\hat{g}_{\mu\nu}$ is smooth at $\mathcal{I}^+$ and, referring to (2.1), takes the form [24]

$$\hat{g}_{\mu\nu}dx^\mu dx^\nu = -(e^{2\beta}V\ell^3 - h_{AB}U^A U^B)du^2 + 2e^{2\beta}du d\ell - 2h_{AB}U^B du dx^A + h_{AB}dx^A dx^B. \tag{2.14}$$

As described in [5], the Bondi news function $N(u, x^A)$ and the Newman-Penrose Weyl tensor component [43]

$$\Psi_4^0(u, x^A) = \lim_{r\to\infty} r\psi_4$$

which describe the waveform are both determined by the asymptotic limit at $\mathcal{I}^+$ of the tensor field

$$\hat{\Sigma}_{\mu\nu} = \frac{1}{\ell}\left(\hat{\nabla}_\mu\hat{\nabla}_\nu - \frac{1}{4}\hat{g}_{\mu\nu}\hat{\nabla}^\alpha\hat{\nabla}_\alpha\right)\ell. \tag{2.15}$$

This limit is constructed from the leading coefficients in an expansion of the metric in powers of ℓ. We thus write

$$h_{AB} = H_{AB} + \ell c_{AB} + O(\ell^2). \tag{2.16}$$

Conditions on the asymptotic expansion of the remaining components of the metric follow from the Einstein equations:

$$\beta = H + O(\ell^2), \tag{2.17}$$

$$U^A = L^A + 2\ell e^{2H}H^{AB}D_B H + O(\ell^2) \tag{2.18}$$

and

$$\ell^2 V = D_A L^A + \ell(e^{2H}\mathcal{R}/2 + D_A D^A e^{2H}) + O(\ell^2), \tag{2.19}$$

where H and L are the asymptotic limits of β and U and where $\mathcal{R}$ and D_A are the 2-dimensional curvature scalar and covariant derivative associated with H_{AB}.

The expansion coefficients H, H_{AB}, c_{AB} and L^A (all functions of u and x^A) completely determine the radiation field. One can further specialize the Bondi coordinates to be *inertial* at $\mathcal{I}^+$, i.e. have Minkowski form, in which case $H = L^A = 0$, $H_{AB} = q_{AB}$ (the unit sphere metric) so that the radiation field is completely determined by c_{AB}. However, the characteristic extraction of the waveform is carried out in computational coordinates determined by the Cauchy data on the extraction worldtube so that this inertial simplification cannot be assumed.

In order to compute the Bondi news function in the $\hat{g}_{\mu\nu}$ frame, it is necessary to determine the conformal factor ω relating H_{AB} to a unit sphere metric Q_{AB}, i.e. to an inertial conformal Bondi frame [24] satisfying

$$Q_{AB} = \omega^2 H_{AB}. \tag{2.20}$$

(See [44] for a discussion of how the news in an arbitrary conformal frame is related to its expression in this inertial Bondi frame.) We can determine ω by solving the elliptic equation governing the conformal transformation of the curvature scalar (2.7) to a unit sphere geometry,

$$\mathcal{R} = 2(\omega^2 + H^{AB} D_A D_B \log\omega). \tag{2.21}$$

Equation (2.21) need only be solved at the initial time. Then the geometrical properties of $\mathcal{I}^+$ determines the time dependence of ω according to

$$2\hat{n}^\alpha \partial_\alpha \log\omega = -e^{-2H} D_A L^A, \tag{2.22}$$

where $\hat{n}^\alpha = \hat{g}^{\alpha\beta}\nabla_\beta \ell$ is the null vector tangent to the generators of $\mathcal{I}^+$. We use (2.22) to evolve ω along the generators of $\mathcal{I}^+$ given a solution of (2.21) as initial condition.

The news function $N(u, x^A)$ is first computed by the code in terms of the computational coordinates (u, x^A), as opposed to the inertial coordinates $(\tilde{u}, y^A)$ on $\mathcal{I}^+$ corresponding to an idealized distant observatory. The transformation to inertial coordinates proceeds by introducing the conformally rescaled metric $\tilde{g}_{\mu\nu} = \omega^2 \hat{g}_{\mu\nu}$ in which the cross-sections of $\mathcal{I}^+$ have unit sphere geometry, in accord with (2.20). The rescaled null vector $\tilde{n}^\nu = \omega^{-1}\hat{n}^\nu$ is then the generator of the inertial time translation on $\mathcal{I}^+$, i.e. $\tilde{n}^\nu \partial_\nu = \partial_{\tilde{u}}$. The inertial coordinates thus satisfy the propagation equations

$$\hat{n}^{\ \nu}\partial_\nu \tilde{u} = \omega, \qquad \hat{n}^\nu \partial_\nu y^A = 0, \tag{2.23}$$

where $\hat{n}^\nu \partial_\nu = e^{-2H}(\partial_u + L^A \partial_{x^A})$ in terms of the computational coordinates. The inertial coordinates are obtained by integrating (2.23), thus establishing a second pair of stereographic grid patches corresponding to y^A. Then the news function is transformed into $N(\tilde{u}, y^A)$. (More precisely, we should write $\tilde{N}(\tilde{u}, y^A) = \hat{N}(u, x^A)$ to distinguish the functional form of the news in the different coordinates but we forgo this complication of notation.)

In addition, in order for the real and imaginary parts of N to correspond to the plus and cross polarization modes of a distant observatory, we need the proper choice of complex polarization vector $\mathcal{Q}^\beta$, which in the inertial coordinates is related to the unit sphere metric on $\mathcal{I}^+$ by $Q^{AB} = (\mathcal{Q}^A \bar{\mathcal{Q}}^B + \bar{\mathcal{Q}}^A \mathcal{Q}^B)/2$. We fix the spin rotation freedom $\mathcal{Q}^\beta \to e^{-i\eta}\mathcal{Q}^\beta$ by requiring $\tilde{n}^\nu \tilde{\nabla}_\nu \mathcal{Q}^\beta = O(\Omega)$, so that the polarization frame is parallel propagated along the inertial time flow on $\mathcal{I}^+$. This fixes the polarization modes determined by the real and imaginary parts of the news to correspond to those of inertial observers at $\mathcal{I}^+$. In order to carry this out in the computational frame we introduce the dyad decomposition $H^{AB} = (F^A \bar{F}^B + \bar{F}^A F^B)/2$ where

$$F^A = q^A \sqrt{\frac{(K+1)}{2}} - \bar{q}^A J \sqrt{\frac{1}{2(K+1)}}. \tag{2.24}$$

We then set $\mathcal{Q}^\beta = e^{-i\delta}\omega^{-1}F^\beta + \lambda \tilde{n}^\beta$, where $F^\alpha := (0, 0, F^A)$. The requirement of an inertial polarization frame, $\tilde{n}^\nu \tilde{\nabla}_\nu \mathcal{Q}^\beta = O(\Omega)$, then determines the time dependence of the phase δ according to

$$2i(\partial_u + L^A \partial_A)\delta = D_A L^A + H_{AC}\bar{F}^C((\partial_u + L^B\partial_B)F^A - F^B \partial_B L^A). \tag{2.25}$$

The Bondi news now takes the explicit form

$$N = \frac{1}{4} e^{-2i\delta}\omega^{-2} e^{-2H} F^A F^B \Big\{ (\partial_u + \mathcal{L}_L) c_{AB} - \frac{1}{2} c_{AB} D_C L^C + 2\omega D_A[\omega^{-2} D_B(\omega e^{2H})] \Big\}, \tag{2.26}$$

where $\mathcal{L}_L$ denotes the Lie derivative with respect to L^A.

In the inertial Bondi coordinates, the expression for the news function reduces to the simple form

$$N = \frac{1}{4} \mathcal{Q}^A \mathcal{Q}^B \partial_u c_{AB}. \tag{2.27}$$

However, the general form (2.26) must be used in the computational coordinates, which is challenging for maintaining accuracy because of the appearance of second angular derivatives of ω.

Alternatively, the waveform can be obtained from the asymptotic value of the Weyl tensor. Asymptotic flatness implies that the Weyl tensor vanishes at $\mathcal{I}^+$, i.e. $\hat{C}_{\mu\nu\rho\sigma} = O(\ell)$ in the $\hat{g}_{\mu\nu}$ conformal Bondi frame (2.14). This is the conformal space version of the peeling property of asymptotically flat spacetimes [23]. Let $(\hat{n}^\mu, \hat{\ell}^\mu, \hat{m}^\mu)$ be an orthonormal null tetrad such that $\hat{n}^\mu = \hat{\nabla}^\mu \ell$ and $\hat{\ell}^\mu \partial_\mu = \partial_\ell$ at $\mathcal{I}^+$. The radiation is described in this frame by the limit

$$\hat{\Psi} := -\frac{1}{2} \lim_{\ell\to 0} \frac{1}{\ell} \hat{n}^\mu \hat{m}^\nu \hat{n}^\rho \hat{m}^\sigma \hat{C}_{\mu\nu\rho\sigma}, \tag{2.28}$$

which in Newman-Penrose notation [43] corresponds to

$$\hat{\Psi} = -(1/2)\bar{\psi}_4^0. \tag{2.29}$$

The limit is independent of how the tetrad is extended off $\mathcal{I}^+$.

A major calculational result in [5] is that

$$\hat{\Psi} = \frac{1}{2} \hat{n}^\mu \hat{m}^\nu \hat{m}^\rho (\hat{\nabla}_\mu \hat{\Sigma}_{\nu\rho} - \hat{\nabla}_\nu \hat{\Sigma}_{\mu\rho})|_{\mathcal{I}^+}, \tag{2.30}$$

where $\hat{\Sigma}_{\alpha\beta}$ is given by (2.15) and where (2.30) is independent of the freedom

$$\hat{m}^{\ \nu} \to \hat{m}^\nu + \lambda \hat{n}^\nu. \tag{2.31}$$

In the same inertial polarization frame used in describing the news,

$$\Psi = \frac{1}{2}\omega^{-3}e^{-2i\delta}\hat{n}^{\mu}F^{A}F^{B}(\partial_{\mu}\hat{\Sigma}_{AB} - \partial_{A}\hat{\Sigma}_{\mu B} - \hat{\Gamma}^{\alpha}_{\mu B}\hat{\Sigma}_{A\alpha} + \hat{\Gamma}^{\alpha}_{AB}\hat{\Sigma}_{\mu\alpha})|_{\mathcal{I}^{+}}. \quad (2.32)$$

An explicit expression for Ψ in terms of the asymptotic metric coefficients involves lengthy algebra which was carried out using a Maple script to write it in terms of $\eth$ operators acting on the spin-weighted computational fields and to construct the final Fortran expression for Ψ.

In inertial Bondi coordinates, (2.32) reduces to the single term

$$\Psi = \frac{1}{4}Q^{A}Q^{B}\partial_{u}^{2}c_{AB} = \partial_{u}^{2}\partial_{l}J|_{\mathcal{I}^{+}}. \quad (2.33)$$

This is related to the expression for the news function in inertial Bondi coordinates by

$$\Psi = \partial_{u}N. \quad (2.34)$$

However, as in the case of the news, the full expression for Ψ obtained from (2.32) must be used in the code. This introduces additional challenges to numerical accuracy due to the large number of terms and the appearance of third angular derivatives.

These difficulties can be appreciated by considering the linearized approximation, for which considerable simplification arises. To first order in a perturbation off a Minkowski background, the nonlinear expression (2.32) for Ψ reduces to

$$\Psi = \frac{1}{2}\partial_{u}^{2}\partial_{\ell}J - \frac{1}{2}\partial_{u}J - \frac{1}{2}\eth L - \frac{1}{8}\eth^{2}(\eth\bar{L} + \bar{\eth}L) + \partial_{u}\eth^{2}H. \quad (2.35)$$

In the same approximation, the news function is given by

$$N = \frac{1}{2}\partial_{u}\partial_{\ell}J + \frac{1}{2}\eth^{2}(\omega + 2H). \quad (2.36)$$

The linearized Einstein equations imply that (2.34), i.e. $\Psi = \partial_{u}N$, still holds in the linearized approximation. (In the nonlinear case, the derivative along the generators of $\mathcal{I}^{+}$ is $\hat{n}^{\nu}\partial_{\nu} = e^{-2H}(\partial_{u} + L^{A}\partial_{A})$ and (2.34) must be modified accordingly.)

The linearized expressions (2.35) and (2.36) provide a starting point to compare the advantages between computing the radiation via the Weyl component Ψ or the news function N. The troublesome terms involve L, H and ω, which all vanish in inertial Bondi coordinates. One main difference is that Ψ contains third order angular derivatives, e.g. the term $\eth^{3}\bar{L}$, as opposed to second angular derivatives in the case of N. This means that smoothness of the numerical error is more crucial in the Ψ approach. Balancing this, another main difference is that N contains the term $\eth^{2}\omega$, which is a potential source of numerical error since ω must be propagated across the stereographic patch boundaries via (2.22). Test comparisons of waveforms obtained via N and Ψ are given in the next section.

III. TESTS OF MODIFICATIONS TO THE STEREOGRAPHIC GRID

The characteristic evolution carried out by the PITT code integrates the Bondi-Sachs equations by means of a finite-difference approximation [25,26]. Stereographic coordinates $x^{A} = (q, p)$ are used to label the angles on the outgoing null cones. In the original code, two square stereographic patches were used, one centered about the North pole and the other about the South pole. In the new stereographic scheme introduced in [5], the patches were modified to have circular boundaries located just past the equator, and angular dissipation was introduced to suppress the short wavelength noise introduced by interpatch interpolation. In addition, in the original code $\eth$-derivatives were approximated by second order accurate finite-difference approximations. In the present version used in this paper, the $\eth$-derivatives have been increased to fourth-order accuracy. Although the overall second-order convergence rate of the PITT code remains unchanged, these changes are expected to lead to more accurate waveforms.

There has been extensive testing of the accuracy of past versions of the code in [5,7,26,31]. Here we repeat some of the linear wave tests presented in [5] in order to demonstrate the improvement obtained by fourth-order accurate angular derivatives. First, in order to verify that the new treatment of stereographic patches is capable of producing a fourth-order accurate evolution, we carry out a test of wave propagation on the sphere based upon solutions to the 2D wave equation

$$-\partial_{t}^{2}\Phi + \eth\bar{\eth}\Phi = 0, \quad (3.1)$$

where $\Phi = \cos(\omega t)Y_{lm}$, $\omega = \sqrt{l(l+1)}$ and Y_{lm} are spherical harmonics. For the case $l = m = 2$ we measure the convergence rate of the error. The simulations are run with $n + 1$ grid points along the axes of each patch, with the grid sizes ranging from $n = 80$ to $n = 240$. For a given grid size, we use the L_{∞} norm to measure the error

$$\mathcal{E}(\Phi) = \|\Phi_{\text{numeric}} - \Phi_{\text{analytic}}\|_{\infty} \quad (3.2)$$

for the circular patches in each hemisphere. We measure the convergence rate for $\mathcal{E}(\Phi)$ at a given time t, for two consecutive grid sizes n_1 and n_2, by

$$\mathcal{R} = \frac{\log_2(\mathcal{E}(\Phi)_{n_2}/\mathcal{E}(\Phi)_{n_1})}{\log_2(n_1/n_2)}. \quad (3.3)$$

Convergence rates for the derivatives are measured analogously.

Excellent fourth-order convergence of $\mathcal{E}(\Phi)$ was obtained. It is more important and challenging for assessing waveform extraction error to measure the error in the derivatives $\eth\Phi$, $\eth^{2}\Phi$, and $\eth^{3}\Phi$, since second angular derivatives enter in the computation of the Bondi news and third angular derivatives enter into the computation of Ψ. The convergence rates, measured with the L_{∞} norm over

TABLE I. Convergence rates for errors in $\eth\Phi$, $\eth^2\Phi$ and $\eth^3\Phi$.

$\mathcal{E}/n$	$n_1 = 80$	$n_1 = 120$	$n_1 = 160$	$n_1 = 200$
$\mathcal{E}(\eth\Phi)$	4.04	4.11	4.35	4.85
$\mathcal{E}(\eth^2\Phi)$	4.07	4.24	4.80	3.95
$\mathcal{E}(\eth^3\Phi)$	3.98	3.95	3.92	3.86

the North patch, are shown in Table I based upon the grid sizes $(n_1, n_2) = (80, 120)$, (120, 160), (160, 200), (200, 240).

For the coarser grids, good fourth-order convergence is apparent for all the derivatives. As the grids are refined, the error eventually approaches (double precision) roundoff error and convergence becomes a moot question.

Next we compare the accuracy of waveform extraction by computing the news function N and the Weyl tensor component Ψ in the test problem considered in [5], which is based upon a periodic, linearized gravitational wave on a Minkowski background (see Sec. 4.3 of [45]). The linearized wave is expressed in Bondi-Sachs coordinates so that it allows direct measurement of the numerical error. The wave has period $T = \pi$ and $(l = 2, m = 0)$ spherical harmonic dependence, with the maximum value of $J \approx 10^{-6}$. The data provided by the linearized solution at the extraction worldtube was propagated to $\mathcal{I}^+$ by the characteristic code, where the waveform was computed and compared to its analytic value. The computational error in the waveform was measured with the L_2 norm over the North patch using the $n = 100$ grid.

Figure 1 compares plots of the error in the real part of the news function N (computed on the North patch) for the second- and fourth-order accurate angular derivatives.

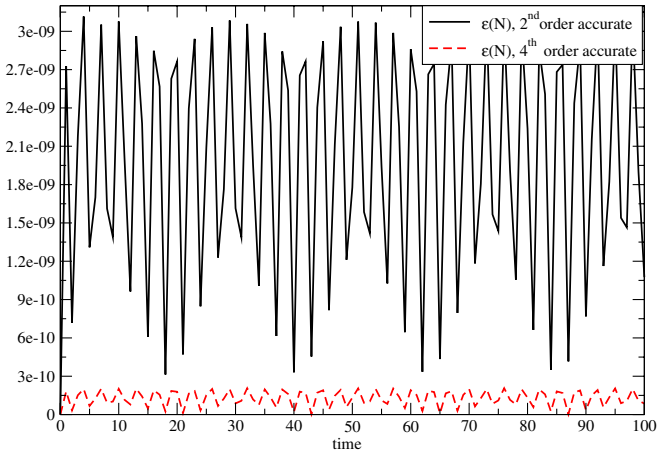

FIG. 1 (color online). Plots of the L_2 errors $\mathcal{E}(N)$ vs t in the real part of the news function extracted in a linearized gravitational wave test. The plots compare the errors obtained using the second- and fourth-order accurate angular derivatives on an $n = 100$ grid. The fourth-order method reduces the error by an order of magnitude. The time variation of the error matches the period of the wave.

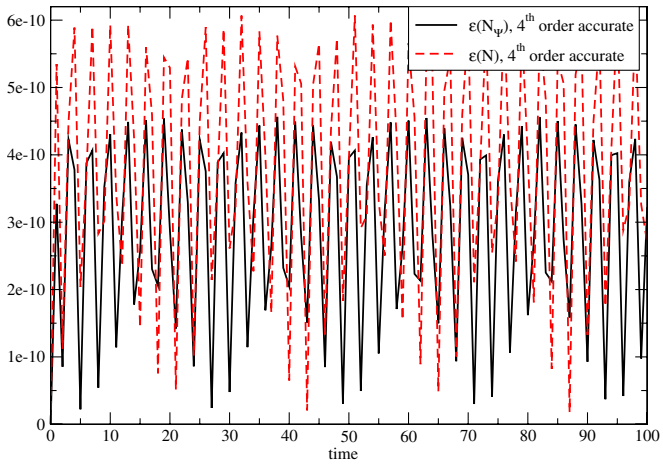

FIG. 2 (color online). Comparison plots of the L_2 errors $\mathcal{E}(N)$ and $\mathcal{E}(N_\Psi)$ vs t in the news function computed directly and via the Weyl tensor for the linearized gravitational wave test. The results were obtained using fourth-order accurate angular derivatives on an $n = 100$ grid. The two methods are competitive although $\mathcal{E}(N_\Psi)$ is slightly smaller in this case.

The plots show roughly one order of magnitude improvement in accuracy for the $n = 100$ grid. The corresponding plots of the error in the waveform measured by the Weyl component Ψ show again roughly one order of magnitude improvement in accuracy. Further improvement in accuracy might be obtained by also increasing the radial derivatives to fourth-order approximations but this could entail nonlinear complications which could affect the numerical stability of the evolution algorithm [42].

In accord with (2.34), the computation of the Weyl component Ψ yields an alternative numerical value for the news

$$N_\Psi = N|_{u=0} + \int_0^u \Psi du, \tag{3.4}$$

where $N = N_\Psi$ in the analytic problem. Figure 2 compares these two extraction methods in terms of the errors in N and N_Ψ for the linearized wave test when using 4th order accurate angular derivatives. The plots show that the two methods are competitive although the error in N_Ψ is slightly smaller in this case.

IV. COMPUTATIONAL INTERFACE

We have designed an interface that takes Cartesian grid data from a Cauchy evolution and converts it into boundary data for a characteristic evolution on a spherical grid extending to $\mathcal{I}^+$. We treat each component $g_{\mu\nu}(t, x^i)$ of the Cauchy metric as a scalar function in the x^i Cartesian coordinates which are used in the $3 + 1$ evolution. In order to make the interface as flexible as possible for use as a community tool for waveform extraction, we have based it upon a spectral decomposition of the Cauchy data in the region between two world tubes or radii $R = R_1$ and

$R = R_2$, where $R = \sqrt{\delta_{ij} x^i x^j}$ is the Cartesian coordinate radius. Then at a given time t, we decompose $g_{\mu\nu}(t, x^i)$ in terms of Chebyshev polynomials of the second kind $U_k(R)$ and spherical harmonics $Y_{lm}(\theta, \phi)$, where (θ, ϕ) are related to x^i/R in the standard way. The Chebyshev polynomials are conventionally defined as functions $U_k(\tau)$ on the interval $-1 \le \tau \le 1$. Here we map them to the interval $R_1 \le R \le R_2$ by the transformation

$$\tau(R) = \frac{2R - R_1 - R_2}{R_2 - R_1}.$$

Thus, for $R_1 < R < R_2$, we expand

$$g_{\mu\nu}(t, x^i) = \sum_{klm} C_{\mu\nu[klm]}(t) U_k(R) Y_{lm}(\theta, \phi). \tag{4.1}$$

For the application to waveform extraction given in this paper, we choose $l \le l\,\mathrm{max}$, where $l\,\mathrm{max} = 6$, and $k \le k_{\mathrm{max}}$, where $k_{\mathrm{max}} = 6$. These values should be considered tentative and further experimentation is warranted to optimize accuracy. In tests of binary black holes with mass M we use a relatively small range $R_2 - R_1 = 10M$ and a larger value of k_{max} would certainly be needed if the range were expanded. Also, while $l\,\mathrm{max} = 6$ might be sufficient for extraction at $R_E = 100M$, a larger value might give improved results at $R_E = 20M$.

The coefficients $C_{\mu\nu[klm]}$ allow us to reconstruct a spherical harmonic decomposition of each component of the Cauchy metric on the extraction worldtube $R = R_E$, i.e.

$$g_{\mu\nu[lm]}(t, R_E) = \sum_k C_{\mu\nu[klm]}(t) U_k(R_E). \tag{4.2}$$

This decomposition is carried out at a sequence of Cauchy time steps $t_n = t_0 + n\Delta t$, where Δt is chosen to be much smaller than the physical time scales in the problem but, for purpose of economy, larger than the time step used for the Cauchy evolution. At each time step, the spectral coefficients are determined by a least squares fit to the Cauchy metric.

The extraction module also requires the derivatives $\partial_t g_{\mu\nu}$ and $\partial_R g_{\mu\nu}$ at the extraction worldtube. The R-derivative is obtained analytically, at each time level t_n, by differentiation of the Chebyshev polynomials. In one option, the finite-difference option, the t-derivative is constructed by a fourth-order accurate finite-difference approximation based upon the sequence of Cauchy times $t = t_n$. In a second option, the fast-Fourier-transform (FFT) option, we modify the Cauchy data by filtering each mode $f_n = C_{klm}(t_n)$ to remove high-frequency noise (both numerical noise and high-frequency gauge waves). The filter works as follows. Let f_n be the original data $(n = 0, \ldots, N-1)$, and $g_n = f_n - a(n\Delta t) - b(n\Delta t)^2$. The coefficients a and b are fixed by requiring that $g_N = g_0$ (where g_N is extrapolated from g_{N-1} and g_{N-2}) and $g_0 - g_{N-1} = g_2 - g_1$, i.e. the one-sided derivatives taken at $n = 0$ agree. This guarantees continuity of g and its first derivative when periodically extended. We then perform a FFT on g_i, truncate the transform at high frequencies, and perform an inverse Fourier transform to obtain a filtered G_n and optionally, the inverse transform of $i\omega g_i$ to obtain a smooth time derivative of G_n. We then construct the filtered mode $C_{klm}(t_n) = G_n + a(n\Delta t) + b(n\Delta t)^2$, as well as its time derivative.

The stereographic coordinates $x^A = (q, p)$ used to label the outgoing null rays in the Bondi metric are matched to the spherical coordinates (θ, ϕ) induced by the Cartesian Cauchy coordinates on the extraction worldtube by a standard transformation, using the conventions in [40]. The value of the surface-area coordinate r in the Bondi-Sachs metric is obtained on the extraction worldtube from the 2-determinant of the Cartesian metric on the surfaces $t = t_n$, $R = R_E$. As a result $r_E(t_n, q, p) := r|_{R=R_E} \ne \mathrm{const}$ on the extraction worldtube. In order to deal with this complication, the transformation from Cartesian coordinates (t, x^i) to Bondi-Sachs coordinates (u, r, x^A) is carried out via an intermediate Sachs coordinate system (u, λ, x^a) [46] where λ is an affine parameter along the outgoing null rays. The affine freedom allows us to set $\lambda = 0$ on the extraction worldtube. After carrying out the Jacobian transformation from (t, x^i) to (u, λ, x^A), the Cartesian metric and its first derivatives at the extraction worldtube provide a first order Taylor expansion in λ (about $\lambda = 0$) of the null metric in Sachs coordinates. The corresponding Taylor expansion of the metric in Bondi-Sachs coordinates then follows from the computed values of r_E and $\partial_\lambda r$ at $\lambda = 0$, which are obtained from the 2-determinant of the Cartesian metric [6].

This allows us to build a grid based upon the characteristic coordinates (x, q, p), with compactified radial coordinate x given by (2.9). The grid values $x_i = x_{i-1} + \Delta x$, $1 \le i \le n_x$, are adjusted so that $x_1 < x_E := x|_{R=R_E}$ and $x_{n_x} = 1$. The characteristic time levels $u_n = u_{n-1} + \Delta u$ are chosen to coincide with the Cauchy times t_n on the extraction worldtube by choosing $(u - t)|_{R=R_E} = 0$.

In the previous version of the extraction module, the first order Taylor expansion for the Bondi metric was used to fill the gridpoints neighboring the extraction worldtube and thus initiate the radial integration of the hypersurface Eqs. (2.3), (2.4), (2.5), and (2.6). However, the hypersurface equations require only 6 (real) integration constants, which can be supplied by their values at $R = R_E$. Using the Taylor expansion to fill the neighboring gridpoints leads to a potential inconsistency between the Bondi metric supplied by the Cauchy evolution and the radial derivatives determined by the characteristic hypersurface and evolution equations. In particular, we have found that such inconsistencies arising from error in the Cauchy data degrade the convergence rate of the characteristic extraction module. Because convergence of the extraction module is an important test of its reliability, we proceed here in a different manner which decouples the Cauchy and characteristic extraction errors.

In the previous version of the extraction module, the Taylor expansions were also applied to the auxiliary variables $\nu = \bar{\eth}J$, $\mathcal{B} = \eth\beta$ and $k = \eth K$ by applying the $\eth$-operator to the Taylor expansions of the main variables. This was a complicated process because the $\eth$ operator intrinsic to the $\lambda = 0$ extraction worldtube is not the same as the $\eth$ operator intrinsic to the $r = \text{const}$ Bondi spheres (as they differ by radial derivatives). In the process, several bugs were introduced in the radial start-up scheme. The present version of the extraction module streamlines the start-up of the auxiliary variables by avoiding the use of Taylor expansions.

In this new approach, the hypersurface equations are integrated purely in terms of the values β_E, Q_E, U_E and W_E of the hypersurface variables on the extraction worldtube which are supplied by the Cauchy data. A mask is set up to identify those radial grid points $i \le B$ (referred to as "B points") for which $x_i - x_E \le \Delta x$. These grid points are "passive" points which do not directly enter in the evolution. Values of the hypersurface variables are assigned at the first active points $i = B + 1$ (referred to as "$B + 1$ points") in the following manner, assuming that the values J_E and J_{B+1} of the evolution variable J are known, as well as the values ν_{B+1} and k_{B+1} of the auxiliary variables. (We address the latter assumption below in describing the start-up of the evolution algorithm.) Proceeding in the hierarchical order of the hypersurface equations, we first use (2.3) to determine β_{B+1} according to

$$\beta_{B+1} = \beta_E + N_\beta[J](r_{B+1} - r_E). \tag{4.3}$$

Because $N_\beta[J]$ only involves J and $\partial_r J$ it may be evaluated at the midpoint between x_E and x_{B+1} so that the resulting error in β_{B+1} is $O(\Delta x^3)$. This also determines the auxiliary variable $\mathcal{B} = \eth\beta$ at the $B + 1$ points provided the $B + 1$ points on the neighboring rays have the same grid value x_i. However, in the case of an irregularly shaped extraction worldtube, there can be exceptions where this neighboring ray is a B point. As a result, in cases where the B points lie close to the boundary of the masked region they can couple to the $B + 1$ points on neighboring rays through the $\eth$ operator. For this reason, we also update B points by the same scheme used for the $B + 1$ points. (If a B point is within a small tolerance of the worldtube, we instead just copy the worldtube value rather than risk an ill-conditioned algorithm.) In this way, the start-up value of the auxiliary variable $\mathcal{B}_{B+1}$ is determined in all cases.

Next in the hierarchy of hypersurface equations, we determine Q_{B+1} in similar fashion. However, $N_Q[J, \beta]$ involves $\mathcal{B} = \eth\beta$ which cannot be determined on the extraction worldtube from the values of β_E (because of the angular variation of r_E discussed above). Consequently, in order to start up the Q-integration we evaluate N_Q at x_{B+1}, where $\mathcal{B}_{B+1}$ is known. This results in an $O(\Delta x^2)$ error in the value of Q_{B+1}. Similar considerations apply to the start-up of the U and W integrations. As a result, the start-up leads to an overall $O(\Delta x^2)$ error in values at x_{B+1}, which is consistent with the global $O(\Delta x^2)$ error resulting from the remaining integration from x_{B+1} to $\mathcal{I}^+$. This radial march to $\mathcal{I}^+$ proceeds in the same way as described in [26,41,42] to determine all variables on the hypersurface.

Having completed the radial march on the hypersurface at time u_{N-1}, the start-up of the integration scheme on $u_n = u_{n-1} + \Delta u$ begins with the determination of $J_{B+1}(u_n)$ from the worldtube data J_E, β_E, Q_E, U_E and W_E on u_N and the fields already determined on u_{N-1}. We determine $J_{B+1}(u_n)$ using a null parallelogram algorithm [47]. The evolution Eq. (2.8) for J can be rewritten as

$$2\partial_u\partial_r\Phi - \partial_r(A\partial_r\Phi) = \text{RHS} \tag{4.4}$$

where $\Phi = rJ$ and $A = V/r = 1 + rW$. This can be integrated over the null parallelogram in the (u, r) subspace bounded by the u_n and u_{n-1} hypersurfaces and by two ingoing characteristics. For constant A, the ingoing characteristics satisfy $r - (Au/2) = \text{const}$. As depicted in Fig. 3, by choosing one ingoing characteristic to pass through r_E on the u_n hypersurface and the other to pass through r_{B+1} on the midpoint between the u_n and u_{n-1} hypersurfaces, we obtain the integral approximation

$$\Phi(u_n, r_-) = \Phi(u_n, r_E) + \Phi(u_{n-1}, r_+) - \Phi(u_{n-1}, r_0) + \frac{\text{RHS}(r_+ - r_0)\Delta u}{2}. \tag{4.5}$$

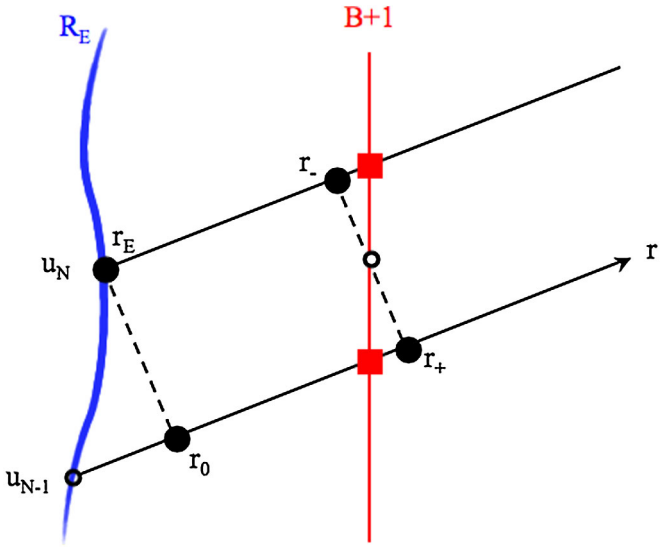

FIG. 3 (color online). The start-up diagram in the (u, r) subspace for the $B + 1$ points (shaded squares). On the left, the extraction worldtube with fixed Cartesian radius R_E moves with respect to the null grid. The null parallelogram for the start-up algorithm is bounded by the two outgoing characteristics at retarded times u_{n-1} and u_n and the two ingoing characteristics indicated by dashed lines. The labels for the radial null coordinate r are indicated at the four corners (shaded circles).

Here the corners of the null parallelogram are located at r_E, $r_\pm = r_{B+1} \pm (A\Delta u/4)$ and $r_0 = r_E + (A\Delta u/2)$; and the center of the null parallelogram is located at $r_c = (1/2)(r_E + r_+)$. This determines the start-up value $\Phi(u_n, r_{B+1})$ through the second-order accurate interpolation

$$\Phi(u_n, r_-) = \frac{[\Phi(u_n, r_{B+1}) - \Phi(u_n, r_E)]r_-}{r_{B+1} - r_E}. \tag{4.6}$$

Using the worldtube data and field values on u_{n-1}, all other quantities can be approximated consistent with second order accuracy except for a term in RHS which is proportional to $\partial_u J$. This term is treated to the required accuracy by a two-step Crank-Nicholson iteration, as is done in the main evolution scheme described in [26]. This leads to a value of $\Phi(u_n, r_{B+1})$, and thus $J(u_n, r_{B+1})$, with $O(\Delta x \Delta u^2)$ error. As in the case of the hypersurface equation, we also use this algorithm to update J at the B points to assure that the auxiliary variables ν_{B+1} and k_{B+1} can be determined by application of the ð operator. Now the radial march continues to the $B + 2$ points by a similar process.

A. Convergence measurements

In tests of the waveform and other variables obtained from a binary black hole evolution there are no exact values available for measuring error so that convergence rates cannot be obtained by use of (3.3). Instead, we obtain Cauchy convergence rates by using measurements obtained with three different gridsizes. For grids in the ratio $\Delta_3 = \chi\Delta_2 = \chi^2\Delta_1$ the Cauchy convergence rate of a measured quantity F is given

$$\mathcal{R} = \frac{\log_2((F_3 - F_2)/(F_2 - F_1))}{\log_2\chi}. \tag{4.7}$$

For quantities that approach the continuum value F_0 as $F = F_0 + G\Delta^2$, (4.7) gives a convergence rate of 2 when G is a smooth function independent of gridsize. In the main part of the characteristic evolution algorithm, G is determined by the second derivatives of the evolution variables. However, a stochastic grid-dependent source of second order error occurs in the start-up algorithm due to the location of the $B + 1$ points. The separation $x_{B+1} - x_E$ of this point from the extraction worldtube can vary discontinuously under a small change in gridsize, i.e. $x_{B+1} - x_E = (1 + \epsilon)\Delta x$, where ϵ is a random number, $0 < \epsilon < 1$. This random separation enters into the second order accurate approximations made in the start-up algorithm. The approach to the continuum value has the form $F = F_0 + (G + \tilde{G}\epsilon)\Delta^2$. Consequently, the stochastic part of the second-order error can obscure the convergence rate determined by (4.7) if $\tilde{G}$ is comparable in size to G. The only way to ensure clean convergence rates would be to implement a third-order accurate start-up algorithm, which would involve a considerable amount of work. Fortunately, this source of error does not appear to be significant in the tests we have carried out. All the main variables exhibit second-order convergence when measured at a finite radius for the results of the binary black hole inspiral presented in Sec. V. However, some asymptotic quantities at $\mathcal{I}^+$ display convergence rates intermediate between first and second order, for reasons discussed further in Sec. V.

B. Constraints on the time step

Domain of dependence considerations place a constraint between the characteristic time step Δu and the size of the characteristic grid analogous to the CFL condition for the Cauchy evolution. For a rough estimate, consider the Minkowski space case with the conformally rescaled metric

$$ds^2 = -\frac{(1-x)^2}{R_E^2}du^2 - \frac{2}{R_E}dudx + q_{AB}dx^A dx^B \tag{4.8}$$

in the compactified stereographic coordinates (u, x, q, p) used in the code, for which the unit sphere metric takes the form

$$q_{AB}dx^A dx^B = \frac{4}{1 + p^2 + q^2}(dp^2 + dq^2). \tag{4.9}$$

The past light cone is determined by

$$\frac{du}{R_E} = \frac{-dx - \sqrt{dx^2 + (1-x)^2 q_{AB}dx^A dx^B}}{(1-x)^2}. \tag{4.10}$$

The restriction on the characteristic time step arising from domain of dependence considerations is strongest at the inner boundary, where $x = 1/2$ (since $r_E = R_E$ in the Minkowski case); and it is also strongest at the equator, where $p^2 + q^2 = 1$. At these points

$$\frac{|du|}{4R_E} = dx + \sqrt{dx^2 + (1/4)(dp^2 + dq^2)}. \tag{4.11}$$

For typical characteristic grid parameters, $\Delta p = \Delta q = \Delta x/4$, the resulting restriction is

$$\frac{|\Delta u|}{R_E} < 8K\Delta x \tag{4.12}$$

where $K \approx 1$ depends upon the details of the finite-difference stencil. This restriction is strongest for a small extraction radius. The characteristic code monitors the corresponding restriction on Δu determined by the curved space version of the compactified Bond-Sachs metric. For a Cauchy simulation of binary black holes with mass M with timestep $\Delta t = M/32$ (sufficient to describe the frequencies typical of a binary system), (4.12) leads to

$$\frac{M}{256R_E} < K\Delta x, \tag{4.13}$$

for the choice of characteristic timestep $\Delta u = \Delta t$. The corresponding number of radial gridpoints must roughly satisfy $n_x < 128R_E/M$. This places no limit of practical

concern on the resolution of the characteristic evolution even for the small extraction radius $R_E = 20M$. Thus, for purposes of CCE, there are no demanding CFL restrictions on the characteristic grid and timestep.

C. Initial characteristic data

The initial data for characteristic evolution consist of the values of J on the hypersurface $u = T_0$. One way of attempting to suppress incoming radiation in this data is to set the Newman-Penrose Weyl tensor component $\psi_0 = 0$ on the initial null hypersurface. For a perturbation of the Schwarzschild metric, this condition implies no incoming radiation in the linearized approximation. The condition that ψ_0 vanish involves two-radial derivatives of J, which in the compactified coordinate $\ell = 1/r$ takes the simple linearized form $\partial_\ell^2 J = 0$. Translated into the computational coordinate $x = 1/(1 + R_E\ell)$, we choose the solution

$$J = \frac{J|_{x_E}(1-x)x_E}{(1-x_E)x}, \tag{4.14}$$

which provides continuity of J with its value determined by Cauchy data at the extraction worldtube. Since this choice of J also vanishes at infinity, the initial slice of $\mathcal{I}^+$ has unit sphere geometry and Eq. (2.21) for the conformal factor has the simple solution $\omega = 1$.

V. BINARY BLACK HOLE MEASUREMENTS AND WAVEFORMS

Here we present test results of waveform extraction from the inspiral and merger of two equal-mass, nonspinning black holes. For the Cauchy evolution we used the LazEv code [48,49] along with the Cactus framework [50] and Carpet [51] mesh refinement driver. LazEV is an eighth-order accurate finite-difference code based upon the Baumgarte-Shapiro-Shibata-Nakamura (BSSN) formulation [19,20] of Einstein's equations, which deals with the internal singularities by the moving puncture approach [48,52]. Our simulation used 9 levels of refinement with finest resolution of $h = M/80.64$, and outer Cauchy boundary at $400M$. The initial data consisted of a close quasicircular black-hole binary with orbital frequency $M\Omega = 0.050$, leading to more than a complete orbit before merger (See [53]). We output the metric data on the extraction worldtube every $\Delta t = M/20$.

In the Cauchy evolution, we extract ψ_4 on spheres of Cartesian radius $R/M = 50, 60, \ldots, 100$ and decompose in spin-weighted (l, m) spherical harmonic modes. We use a perturbative formula [54] to extrapolate the perturbative waveform $R\psi_4$ to $R = \infty$,

$$\lim_{R\to\infty}[R\psi_4^{lm}(R,t)] = r\psi_4^{lm}(r,t) - \frac{(l-1)(l+2)}{2} \times \int_0^t dt\,\psi_4^{lm}(r,\tau)d\tau + \mathcal{O}(r^2), \tag{5.1}$$

where r is the areal radius corresponding to the Cauchy extraction radius R. The extrapolation of the perturbative waveform to infinity removes cumulative phase error which otherwise would be introduced by redshift effects.

We present results for the characteristic extracted waveform either in terms of Ψ, related to the Bondi news by $\Psi = \partial_u N$, or, when comparing to the perturbative waveform, in terms of the Newman-Penrose component $\Psi_4 = -2\bar{\Psi}$. For illustrative purposes, we concentrate on the dominant $(l = 2,\ m = 2)$ and subdominant $(l = 4,\ m = 4)$ spherical harmonic modes.

The highest resolution black hole waveform extraction test was run with the following characteristic grid specifications: angular gridpoints $n_q = n_p = 200$, radial gridpoints $n_x = 224$. For convergence tests, we also used grids $n_q = n_p = 100$, $n_x = 112$ and $n_q = n_p = 50$, $n_x = 56$, so that the grid sizes were in the ratio $\chi = 2$. We refer to these as the $n = 200$, 100 and 50 grids, respectively, The characteristic time steps used for these grids were $\Delta t = M/20(n = 200)$, $\Delta t = M/10(n = 100)$ and $\Delta t = M/5(n = 50)$. The characteristic extraction was carried out using worldtube radii $R_E = 20M$, $50M$ and $100M$.

The Pitt null code was run on stereographic patches with circular boundaries using the auxiliary variables (2.10) to eliminate any second derivatives in the angular directions and using 4th order accurate angular derivatives. Angular dissipation was added with the coefficients $\epsilon_x = 10^{-3}$, $\epsilon_u = 10^{-4}$, $\epsilon_Q = \epsilon_W = 10^{-6}$, in the notation of [5].

The best accuracy was obtained using the FFT option to obtain time derivatives of the worldtube data, as described in Sec. IV. For strong signals, e.g. the dominant $(l = 2,\ m = 2)$ spherical harmonic mode, the finite-difference and FFT options are in good agreement. However, for weak signals, e.g. the $(l = 4,\ m = 4)$ mode, the finite-difference option can generate noticeable high-frequency error. See Fig. 4 for a comparison of waveforms computed with the two options. One likely source of the high-frequency error with the finite-difference option is the stochastic error introduced at each time level t_n on the extraction worldtube by the least squares fit of the Cauchy data to the spectral expansion. In the finite-difference option, this error is amplified when taking the time derivatives necessary to compute the waveform and becomes more prominent for short characteristic timesteps. It also becomes more prominent as the extraction radius is increased, in which case the extracted worldtube data is smaller. Similar high-frequency noise is apparent in the worldtube data so that this error cannot be removed by refining the characteristic grid. However, the filtering intrinsic to the FFT option is effective in reducing this error. The remaining results reported in this paper were obtained with the FFT option.

Convergence rates were measured for the $(l = 2,\ m = 2)$ spherical harmonic mode, which is the dominant mode in the waveform. Table II gives the rates for the evolution variables measured on a sphere at Bondi radius

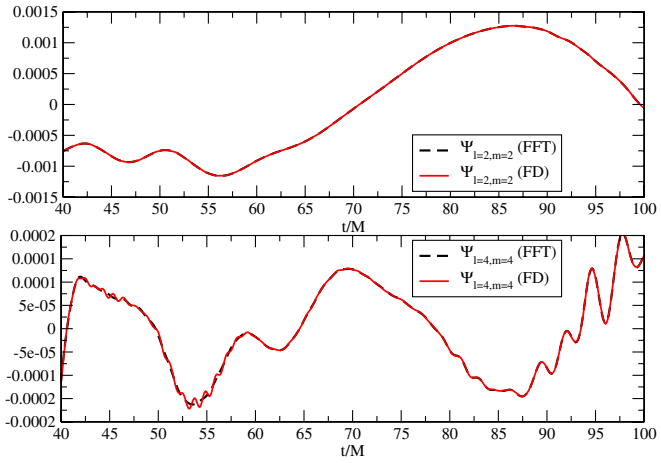

FIG. 4 (color online). Comparison of the finite-difference and FFT options for the (2, 2) (up) and (4, 4) (down) spherical harmonic modes of the real part of the characteristic waveform Ψ obtained with the $n = 200$ grid and extraction radius $R_E = 20M$. The two options give comparable results for the (2, 2) mode but for the (4, 4), which is an order of magnitude smaller, high-frequency error in the worldtube data is noticeable in the waveform extracted with the FD option.

$r = 80M$ obtained with a small extraction radius $R_E = 20M$ at a time corresponding to the peak of the signal ($t \approx 200M$). The rates are given for the real and imaginary part of the variables. All quantities are very close to second order convergent, including $J_{,x}$, which is the term which determines the waveform after transforming to inertial Bondi coordinates according to (2.33).

Table III gives the corresponding convergence rates for these evolution variables measured at $\mathcal{I}^+$, again at the time corresponding to the peak of the signal and with extraction radius $R_E = 20M$. In this case Q and W show deviation from second order convergence, consistent with the asymptotic error analysis presented in Sec. II in relation to (2.13). We also see that the derivative $J_{,x}$ deviates from second order convergence, which indicates a need for more accurate finite-difference approximations near $\mathcal{I}^+$. There are

TABLE II. Convergence rates of the ($l = 2$, $m = 2$) spherical harmonic mode on the sphere $r = 80M$ for the metric variables measured at retarded time $u \approx 200M$ near the peak of the signal. The rates are given for the real and imaginary part of the variables. The extraction radius was $R = 20M$. The results show that the evolution variables all display clean second order convergence.

Variable	Rate_{Re}	Rate_{Im}
β	2.01	2.01
J	2.23	2.01
$J_{,x}$	2.03	2.33
Q	2.02	2.04
U	1.99	1.96
W	1.97	2.00

TABLE III. Convergence rates of the ($l = 2$, $m = 2$) mode for the metric variables measured near the peak of the signal at $\mathcal{I}^+$, with an extraction radius $R = 20M$. As expected from the analysis in Sec. II, some asymptotic quantities only display first order convergence.

Variable	Rate_{Re}	Rate_{Im}
β	2.01	2.01
J	1.80	2.18
$J_{,x}$	1.23	1.20
Q	1.33	1.19
U	1.99	1.96
W	1.55	1.50

several places in the present code where one-sided difference approximations are used for derivatives at $\mathcal{I}^+$. These convergence rates at the peak of the signal are representative of the rates over the entire run. This is illustrated in Fig. 5 which plots the rescaled errors of ReJ and ImQ versus time at $\mathcal{I}^+$.

Table IV gives the corresponding convergence rates for the waveform as measured by the Bondi news N and the Weyl component Ψ, again at a time corresponding to the peak of the signal and with extraction radius $R_E = 20M$. We also show the convergence rate of the inertial time derivative $\partial_u N$ calculated directly from finite differencing N. All show roughly first-order convergence. The rate for $\partial_u N$ is slightly better than that for Ψ, although $\Psi = \partial_u N$ in the continuum limit. The convergence rates of these quantities are affected by two chief factors: (i) the large

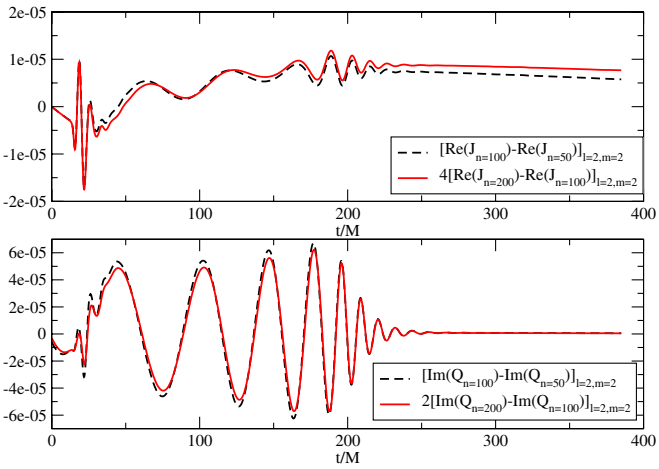

FIG. 5 (color online). Convergence plots of the asymptotic limits at $\mathcal{I}^+$ of the (2, 2) spherical harmonic modes of ReJ and ImQ obtained with resolutions $n = 50$, $n = 100$ and $n = 200$ with an extraction radius $R_E = 20M$. The plots for ReJ are rescaled for second-order convergence (upper plot), while the plots for ImQ (lower plot) are rescaled for first-order convergence. The rescaled differences show that convergence rates at the peak of the signal given in Table III are representative of the rates over the entire run.

TABLE IV. Convergence rates of the (2, 2) spherical harmonic mode for the Bondi news N, $\partial_u N$ obtained by finite-difference, and the Weyl component Ψ, all measured near the peak of the signal with an extraction radius $R_E = 20M$.

Variable	Rate_{Re}	Rate_{Im}
N	1.59	1.56
$\partial_u N$	1.57	1.55
Ψ	1.16	1.14

number of terms involved in their calculation and (ii) their dependence on radial derivatives of the evolution quantities at $\mathcal{I}^+$. In all cases, one-sided approximations are used in several places to compute these radial derivatives. This is already apparent in the convergence rate for $J_{,x}$ shown in Table III.

Surface plots of the Bondi news N and Weyl component Ψ, measured near the peak of the signal with an extraction radius $R_E = 20M$, are shown in Figs. 6 and 7. Both figures display smooth angular dependence, showing that the angular dissipation is effective at removing short wavelength angular noise. In particular, there are no "spikes" near the equatorial patch boundary arising from interpatch interpolation. The main error in the waveform originates from intrinsically time dependent error in the data on the extraction worldtube.

The time dependence of the real part of the characteristic extracted waveform and its comparison to the perturbative waveform are shown in Figs. 8 and 9. Figure 8 shows excellent agreement between these waveforms for the dominant ($l = 2$, $m = 2$) mode, when both are extracted at $R = 50M$. The insets show that this agreement exists in the early stages, when the amplitude is small, and persists throughout the final ringdown. Note that the perturbative

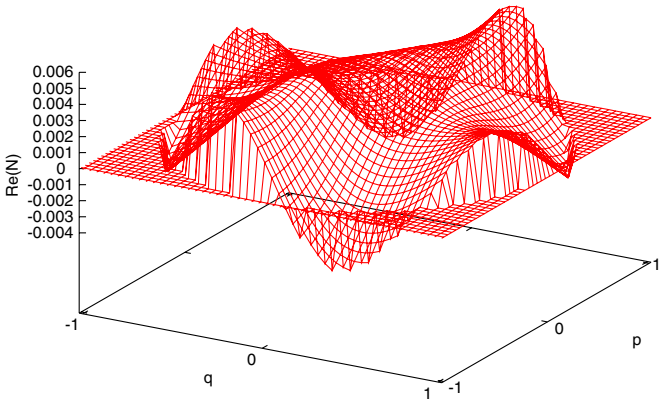

FIG. 6 (color online). Surface plot in the North (q, p) stereographic patch of the real part of the Bondi news N measured at the peak of the wave with an extraction radius $R_E = 20M$. The equatorial patch boundary corresponds to the circle $p^2 + q^2 = 1$. The smooth angular dependence near the equator shows that angular dissipation is effective at removing short wavelength noise arising from interpatch interpolation.

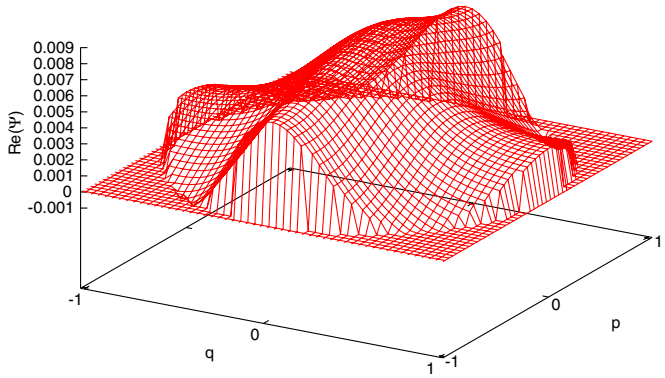

FIG. 7 (color online). Surface plot in the North (q, p) stereographic patch of the real part of the Weyl component Ψ measured at the peak of the wave with an extraction radius $R_E = 20M$. The smooth angular dependence near the equator $p^2 + q^2 = 1$ shows that angular dissipation is effective at removing short wavelength noise arising from interpatch interpolation.

extrapolation formula (5.1) is essential to obtain this excellent phase agreement between the perturbative and characteristic waveforms.

Figure 9 compares the characteristic and perturbative waveforms for the ($l = 4$, $m = 4$) mode. In this case, the perturbative waveform is again extracted at $R = 50M$ but the characteristic waveform is extracted at $20M$ to reduce the high-frequency noise discussed previously. This high-frequency noise can also be reduced by choosing a larger timestep for the characteristic evolution, again indicating that it arises from time derivatives of the stochastic error

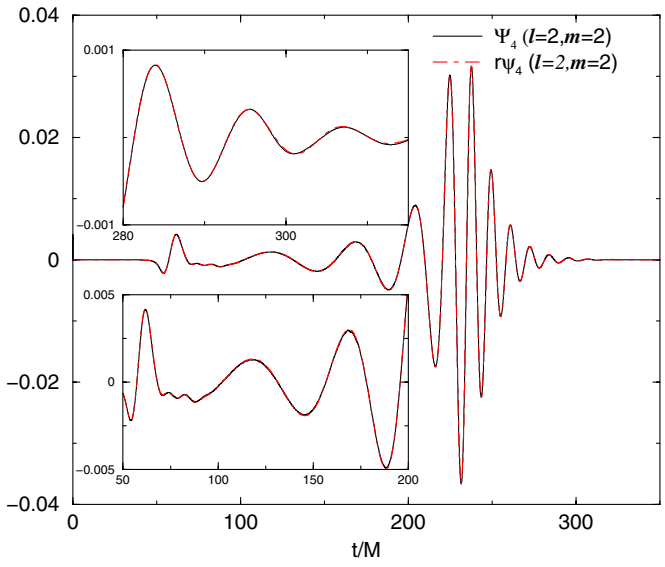

FIG. 8 (color online). Comparison of the (2, 2) dominant spherical harmonic mode for Ψ_4 (characteristic) and $r\psi_4$ (perturbative Cauchy), both extracted at $R = 50M$. The insets show that the excellent agreement extends to the early stages and the final ringdown when the amplitude is small.

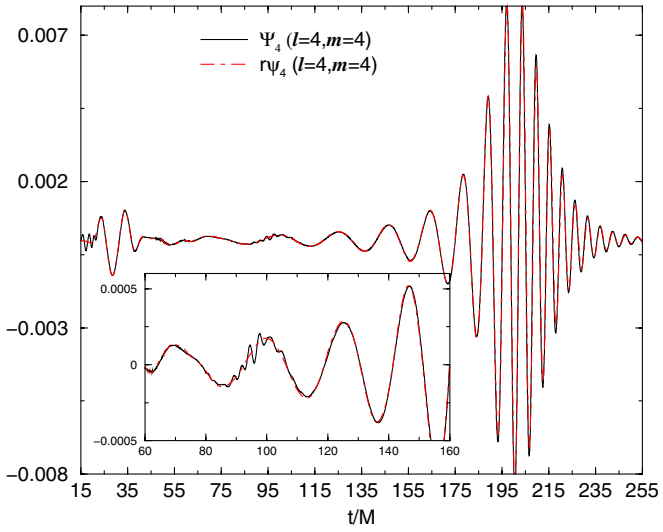

FIG. 9 (color online). Comparison of the (4, 4) subdominant mode for Ψ_4 (characteristic) extracted at $R_E = 20M$ and $r\psi_4$ (perturbative Cauchy) extracted at $R = 50M$. There is good agreement in the strong amplitude regime of the wave $t/M > 120$. At early times $t/M \approx 15$, the characteristic waveform exhibits effects of junk radiation in the initial data near $R_E = 20M$. In addition, the insert magnifies an anomalous feature, which is not fully understood, in the interval about $t/M = 90$.

introduced in the worldtube data by the least squares fit. The characteristic and perturbative waveforms again show excellent agreement At very early times $t/M \approx 15$, the characteristic waveform shows an anomalous feature which can be attributed to "junk" radiation content in the initial data in the vicinity of $R_E = 20M$. In addition, as shown in the insert, there is another anomalous feature, which is not understood, in the time interval about $t/M = 90$. This feature is also evident in the extracted Cauchy data at $R_E = 20M$. Possible sources for this feature are gauge modes excited in the interior region or numerical effects from the adaptive mesh refinement used in the Cauchy evolution. A better explanation would require further runs.

VI. RICHARDSON EXTRAPOLATION AND CONVERGENCE OF THE WAVEFORM

The clean first-order convergence results for the news N and Weyl component Ψ allows us to apply Richardson extrapolation to obtain higher order accuracy waveforms. We apply the results from the three different resolutions $n = (50, 100, 200)$, with grid spacing $(4\Delta, 2\Delta, \Delta)$ respectively, to obtain a third order accurate waveform as follows.

The truncation error in a quantity F can be represented by a power series

$$F(\Delta) = F_0 + F'\Delta + \frac{1}{2}F''\Delta^2 + O(\Delta^3).$$

We write $F_1 = f(\Delta)$, $F_2 = F(2\Delta)$ $F_4 = F(4\Delta)$. Then the extrapolated value

$$F_E = \frac{8}{3}F_1 - 2F_2 + \frac{1}{3}F_4$$

is 3rd order accurate, i.e.

$$F_E = F_0 + +O(\Delta^3).$$

In practice this can be confirmed as follows. Let $F_I = 2F_1 - F_2$ and $F_{II} = 2F_2 - F_4$ be the second order accurate waveforms obtained using data from two resolutions. Then $F_{II} - F_E = 4(F_I - F_E) + O(\Delta^3)$, i.e.

$$\frac{1}{4}(F_{II} - F_E) = F_I - F_E \tag{6.1}$$

if we neglect the $O(\Delta^3)$ error, i.e. if we approximate the exact value F_0 by the third order accurate approximation F_E.

Using the corresponding notation (N_E, N_I, N_{II}) for the news and $(\Psi_E, \Psi_I, \Psi_{II})$ for the Weyl component, we can check the validity of applying Richardson extrapolation to the waveform. Figs. 10 and 11 graph the rescaled errors of the real and imaginary parts of $N_I(t) - N_E(t)$ and $\frac{1}{4}(N_{II}(t) - N_E(t))$ and Fig. 12 graphs the corresponding rescaled errors in $\Psi(t)$. In both cases, (6.1) is confirmed.

These results validate the use of Richardson extrapolation to obtain third order accurate waveforms N_E and Ψ_E. We can use N_E and Ψ_E as fiducial exact values and estimate the truncation error in the numerical waveforms by comparing them with the second order accurate approximates N_I and Ψ_I. Thus the truncation errors in the news N and Weyl component Ψ are conservatively given by

$$\delta N = N_I - N_E = O(\Delta^2) \tag{6.2}$$

and

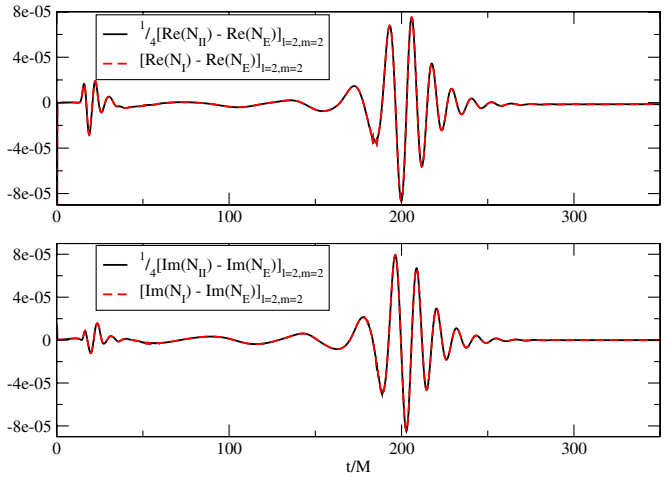

FIG. 10 (color online). Plots confirming the validity of Richardson extrapolation to obtain higher order accuracy for the real and imaginary parts of the dominant (2, 2) spherical harmonic mode of the news $N(t)$. The rescaled errors show that N_I and N_{II} are second order accurate in accord with (6.1).

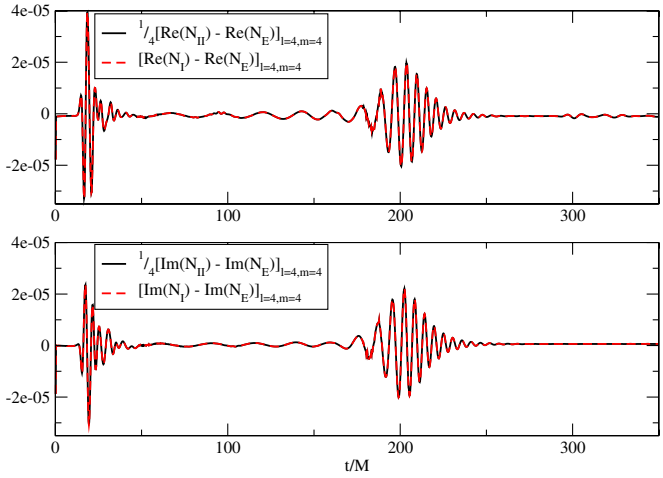

FIG. 11 (color online). Plots confirming the validity of Richardson extrapolation to obtain higher order accuracy for the subdominant (4, 4) spherical harmonic mode of the news $N(t)$. The rescaled errors show again that N_I and N_{II} are second order accurate in accord with (6.1).

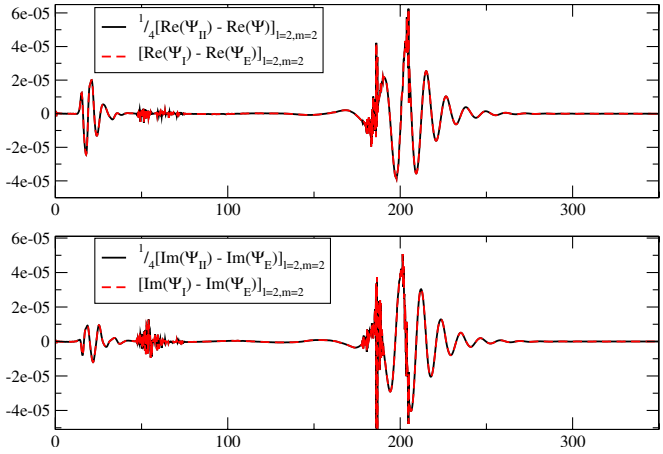

FIG. 12 (color online). Plots confirming the validity of Richardson extrapolation to obtain higher order accuracy for the real and imaginary parts of the (2, 2) spherical harmonic mode of the waveform $\Psi(t)$. The rescaled errors show that Ψ_I and Ψ_{II} are second order accurate in accord with (6.1). Note that the second-order error in Ψ contains more high-frequency noise than N shown in Fig. 10.

$$\delta\Psi = \Psi_I - \Psi_E = O(\Delta^2). \tag{6.3}$$

Figure 13 plots the differences between the dominant $(l = 2, m = 2)$ mode of the Richardson extrapolated waveform $N_E(t)$ obtained with extraction radii $R_E = 20M$, $R_E = 50M$ and $R_E = 100M$. In the plot, the $R_E = 20M$ waveform begins at $t = 0$ and the other waveforms have been shifted backwards in time so that all three are in phase at the peak of the wave. Two sources of extraneous junk radiation can be seen in the figure. One arises from a *mismatch* between the initial characteristic and Cauchy

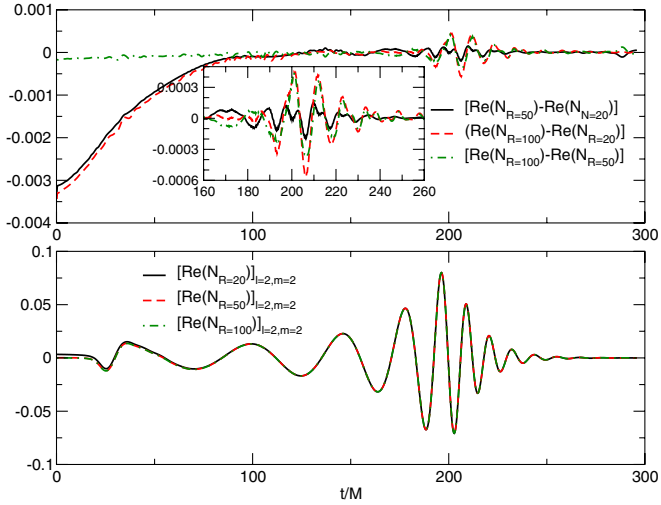

FIG. 13 (color online). Plots of the (2, 2) mode of ReN obtained for extraction radii $R_E = 20M$, $50M$, and $100M$. The $R_E = 50M$ and $R_E = 100M$ waveforms have been shifted backward in time so that they are in phase at the peak of the wave. The noticeable difference in the interval from $t/M = 0$ to $t/M = 100$ between the $R_E = 20M$ waveform and the other two results from a mismatch between the initial characteristic and Cauchy data, which decreases with large extraction radii. For the waveforms extracted at all three radii, the double hump in the interval from $t/M = 0$ to $t/M = 100$ results from nontrivial junk radiation in the initial Cauchy data. The three waveforms are in good agreement in the inspiral and merger stage. At the peak of the wave, the relative difference between the $R_E = 20M$ and $R_E = 100M$ waveforms is less than 0.6%.

data. The initial characteristic data $\psi_0 = 0$ (see Sec. IV C) implies the absence of initial radiation content on the assumption that the geometry of the initial null hypersurface is close to Schwarzschild. This assumption becomes valid as the extraction radius becomes large and the exterior Cauchy data can be approximated by Schwarzschild data. Thus this mismatch is largest for extraction at $R_E = 20M$. This results in a noticeable difference at very early times between extraction at $R_E = 20M$ and the other two radii. After $t/M \approx 100$, the three waveforms are in good agreement with their relative differences less than 0.6% at the peak of the wave.

The second source of junk radiation apparent in Fig. 13 arises from the choice of conformally flat initial Cauchy data. This arises for all three extraction radii and accounts for the double hump in the news function in the interval from $t/M = 0$ to $t/M = 50$.

It is of interest to measure the difference

$$\delta\psi_4 = \left(\frac{1}{2}r\psi_4 + \bar{\Psi}\right) \tag{6.4}$$

between the extracted waveform using the perturbative extrapolation formula (5.1) and the Richardson extrapolated characteristic waveform, measured in accord with the normalization conventions indicated in (2.29). Figure 14

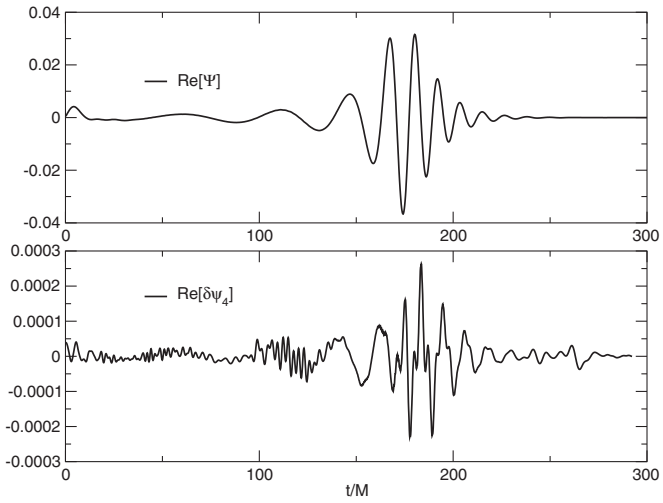

FIG. 14. Plots of the time dependence of the real part of the (2, 2) spherical harmonic components of $\delta\psi_4(t)$, as defined in (6.4), and the characteristic waveform $\Psi(t)$. Here $\delta\psi_4(t)$ measures the difference between the perturbative and characteristic values of $\Psi(t)$. The approximate 1% ratio between the peak amplitudes of $\delta\psi_4(t)$ and Ψ gives an estimate of the difference between perturbative and characteristic extraction.

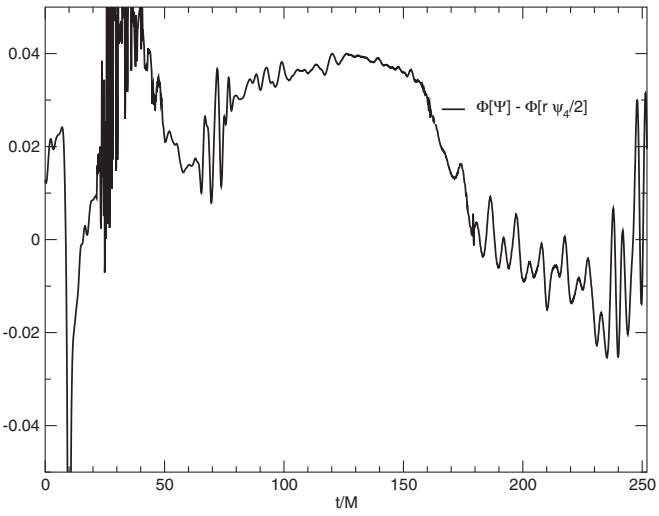

FIG. 15. Plot of the time dependence of the difference in phase $\delta\Phi$, measured in radians, between the ($l = 2$, $m = 2$) components of the characteristic waveform $\Psi(t)$ and the perturbative waveform $r\psi_4(t)/2$. The phase differences are less than 0.05 radians in the interval $40M < t < 250M$ beginning after the initial burst of junk radiation and extending into the late ringdown. The phase errors become large at late times when the numerical noise is comparable to the true signal amplitude and at very early times due the inability of the codes to accurately model the relatively high-frequency initial data burst.

plots the real part of the (2, 2) spherical harmonic component of $\delta\psi_4(t)$, compared with the corresponding component of $\mathrm{Re}\Psi$. The peak amplitude of $\delta\psi_4(t)$ is approximately 1% of the peak amplitude of Ψ, which provides an estimate of the difference between perturbative and characteristic extraction.

Figure 15 plots the phase difference $\delta\Phi$ between the (2, 2) spherical harmonic components of $r\psi_4(t)/2$ and $\Psi(t)$, i.e

$$\delta\Phi = \Phi[\Psi] - \Phi[\psi_4], \tag{6.5}$$

where e.g. $\Psi = |\Psi|e^{i\Phi[\Psi]}$. The phase difference is less than 0.05 radians in the interval $40M < t < 250M$ beginning after the initial burst of junk radiation and extending into the late ringdown. The phase errors become large at late times when the numerical noise in the waveform is comparable to the true signal amplitude and at very early times due to the inability of the codes to accurately model the relatively high-frequency initial data burst.

Note that the magnitude and phase differences between ψ_4 extraction and characteristic extraction indicated in Figs. 14 and 15 are based upon the perturbative extrapolation formula (5.1). It is also common practice to compute ψ_4 at large radii and then extrapolate the values to infinity, cf. the waveform comparisons in the report of the Samurai project [55]. In carrying out the extrapolation, the waveforms are translated by r^*, where $r^* = r + 2M\log(r/2M - 1)$ is the tortoise coordinate obtained from the areal radius of the extraction sphere r and M is the ADM mass of the system [56]. Here we use a linear extrapolation based upon waveforms at $R = 50M$ and

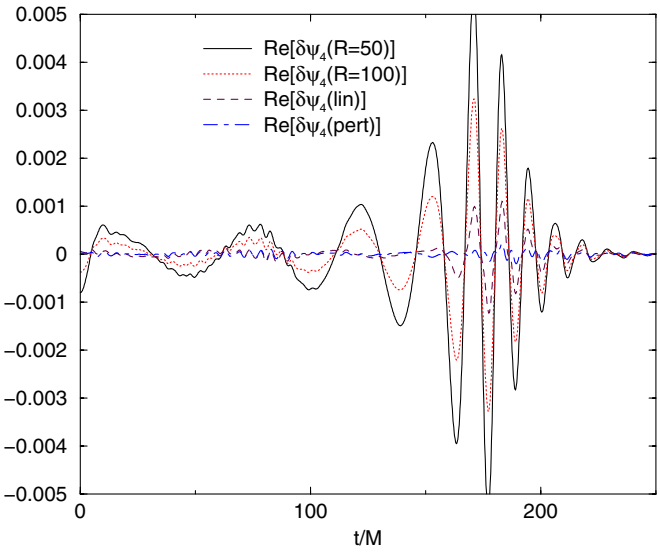

FIG. 16 (color online). Plots of the time dependence of the difference $\mathrm{Re}[\delta\psi_4]$ between the ($l = 2$, $m = 2$) components of the characteristic waveform $\Psi(t)$ and the Cauchy ψ_4 waveforms extracted at $R = 50M$ and $R = 100M$, and their linear extrapolation to $R = \infty$ (denoted by "lin"). For comparison, we also include the corresponding difference (denoted by "pert") using the perturbative extrapolation (5.1). The plots show the expected trend toward smaller errors as $R \to \infty$. Interestingly, perturbative extrapolation, which uses only the $R = 100M$ extraction sphere, gives the smallest deviation.

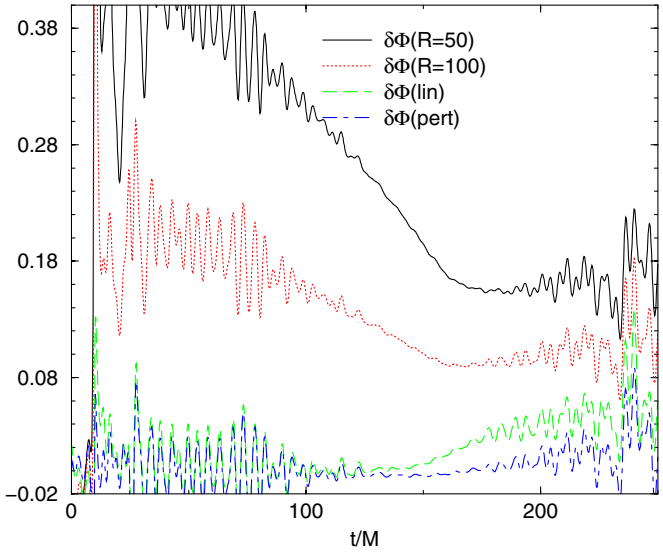

FIG. 17 (color online). Plots of the time dependence of the phase difference $\delta\Phi$ between the ($l = 2$, $m = 2$) components of the characteristic waveform $\Psi(t)$ and the Cauchy ψ_4 waveforms extracted at $R = 50M$ and $R = 100M$, and the corresponding linear extrapolation to $R = \infty$ (denoted by lin). For comparison, we also include the corresponding $\delta\Phi$ (denoted by pert) obtained by perturbative extrapolation (5.1). The plots show the expected trend toward smaller errors as $R \to \infty$. Interestingly, perturbative extrapolation, which uses only the $R = 100M$ extraction sphere, gives the smallest deviation.

$R = 100M$ to obtain an extrapolation $r\psi_4(\text{lin})$ on $\mathcal{I}^+$ that is accurate to order $O(1/R^2)$. The deviations from the characteristic waveform are displayed in Fig. 16, where we plot $\text{Re}[\delta\psi_4(R = 50M)]$, $\text{Re}[\delta\psi_4(R = 100M)]$ and $\text{Re}[\delta\psi_4(\text{lin})]$ and in Fig. 17, where we plot the phase differences $\delta\Phi(R = 50M)$, $\delta\Phi(R = 100M)$ and $\delta\Phi(\text{lin})$. The plots show how the deviations decrease with extraction radius. Linear extrapolation considerably reduces the deviation but it is interesting that perturbative extrapolation via (5.1), which is based upon the single $R = 100M$ result, gives the smallest deviation.

As we discuss next, such time domain comparisons can be of deceptive value for gravitational wave data analysis.

VII. ADVANCED LIGO ACCURACY STANDARDS

It has been emphasized [57] that the direct use of time domain errors would be an abuse of the accuracy standards required of model waveforms to be suitable for gravitational wave data analysis. The raw error envelopes $\delta N(t)$, $\delta\Psi(t)$ and $\delta\psi_4(t)$ cannot be used to test whether the accuracy standards are satisfied. Proper accuracy standards must take into account the power spectral density of the detector noise $S_n(f)$, which is calibrated with respect to the frequency domain strain $\hat{h}(f)$. Consequently, the primary accuracy standards must be formulated in the frequency domain in order to take detector sensitivity into account. Fortunately, for the purpose of calibrating waveforms from numerical simulations, it has been possible to translate the frequency domain accuracy requirements into requirements on the time domain L_2 error norms which meet all the needed criteria [1,37].

There are two distinct criteria for waveform accuracy. First, if the numerical waveform were not sufficiently accurate then an unacceptable fraction of real signals would pass undetected through the corresponding filter. Second, the accuracy impacts on whether a detected waveform measures the physical properties of the source, e.g. mass and spin, to a level commensurate with the accuracy of the observational data. The accuracy standards for model waveforms have been formulated to prevent these potential losses in the detection and scientific measurement of gravitational waves.

For a numerical waveform with strain component $h(t)$, the time domain error is measured by

$$\mathcal{E}_0 = \frac{\|\delta h\|}{\|h\|}, \tag{7.1}$$

where δh is the error in the numerical approximation and $\|F\|^2 = \int dt|F(t)|^2$, i.e. $\|F\|$ is the L_2 norm, which in principle should be integrated over the complete time domain of the model waveform obtained by splicing a perturbative chirp waveform to a numerical waveform for the inspiral and merger.

The error can also be measured in terms of time derivatives of the strain. In our case, the first time derivative corresponds to the error in the news

$$\mathcal{E}_1(\text{Re}N) = \frac{\|\delta\text{Re}N\|}{\|\text{Re}N\|}, \qquad \mathcal{E}_1(\text{Im}N) = \frac{\|\delta\text{Im}N\|}{\|\text{Im}N\|} \tag{7.2}$$

and the second time derivative corresponds to the Weyl component error

$$\mathcal{E}_2(\text{Re}\Psi) = \frac{\|\delta\text{Re}\Psi\|}{\|\text{Re}\Psi\|}, \qquad \mathcal{E}_2(\text{Im}\Psi) = \frac{\|\delta\text{Im}\Psi\|}{\|\text{Im}\Psi\|}. \tag{7.3}$$

Here we measure δN and $\delta\Psi$ according to (6.2) and (6.3) and use the 3rd order Richardson extrapolations to compute $\|\text{Re}N\|$, $\|\text{Im}N\|$, $\|\text{Re}\Psi\|$ and $\|\text{Im}\Psi\|$. It is also of interest to measure the "error"

$$\mathcal{E}_2(\text{Re}\delta\psi) = \frac{\|\text{Re}\delta\psi_4\|}{\|\text{Re}\Psi\|}, \qquad \mathcal{E}_2(\text{Im}\delta\psi) = \frac{\|\text{Im}\delta\psi_4\|}{\|\text{Im}\Psi\|} \tag{7.4}$$

corresponding to the difference between perturbative and characteristic extraction, where $\delta\psi_4$ is normalized according to (6.4).

In [1], it was shown that sufficient conditions to satisfy data analysis criteria for detection and measurement can be formulated in terms of any of the error norms $\mathcal{E}_k = (\mathcal{E}_0, \mathcal{E}_1, \mathcal{E}_2)$, i.e. in terms of the strain, the news or the Weyl component. The accuracy requirement derived in [1] for detection is

$$\mathcal{E}_k \leq C_k \sqrt{2\epsilon_{\max}}, \tag{7.5}$$

and the requirement for measurement is

$$\mathcal{E}_k \leq C_k \frac{\eta_c}{\rho}. \tag{7.6}$$

Here ρ is the optimal signal-to-noise ratio of the detector, defined by

$$\rho^2 = \int_0^\infty \frac{4|\hat{h}(f)|^2}{S_n(f)} df; \tag{7.7}$$

C_k are dimensionless factors introduced in [1] to rescale the traditional signal-to-noise ratio ρ in making the transition from frequency domain standards to time domain standards; $\epsilon_{\max}$ determines the fraction of detections lost due to template mismatch, cf. Eq. (14) of [37]; and $\eta_c \leq 1$ corrects for error introduced in detector calibration. These requirements for detection and measurement, for either $k = 0, 1, 2$, conservatively overstate the basic frequency domain requirements by replacing $S_n(f)$ by its minimum value in transforming to the time domain.

The values of C_k for the inspiral and merger of nonspinning, equal-mass black holes have been calculated in [1] for the advanced LIGO noise spectrum. As the total mass of the binary varies from $0 \rightarrow \infty$, C_0 varies between $.65 > C_0 > 0$, C_1 varies between $.24 < C_1 < .8$ and C_2 varies between $0 < C_2 < 1$. Thus only the error $\mathcal{E}_1$ in the news can satisfy the criteria over the entire mass range. The error in the strain $\mathcal{E}_0$ provides the easiest way to satisfy the criteria in the low mass case $M \ll M_\odot$ and the error in the Weyl component $\mathcal{E}_2$ provides the easiest way to satisfy the criteria in the high mass case $M \gg M_\odot$.

We first concentrate on the error in the news, for which the accuracy requirement for detection is

$$\mathcal{E}_1 \leq C_1 \sqrt{2\epsilon_{\max}}, \tag{7.8}$$

and the requirement for measurement is

$$\mathcal{E}_1 \leq C_1 \frac{\eta_c}{\rho}. \tag{7.9}$$

Table V gives values of several versions of the $\mathcal{E}_1$ error for the inspiral and merger of nonspinning, equal-mass black holes described in Sec. V. For practical purposes, the error norms were computed over the time period of the simulation rather than for a complete model waveform obtained by splicing to a post-Newtonian chirp waveform. Assuming that the nonlinear error in the chirp waveform is small compared to the error in the numerical waveform, the effect is to overestimate the error norms by underestimating the denominators in (7.1), (7.2), and (7.3). However, it has been pointed out in [58,59] that splicing to a chirp waveform can produce significant error unless the numerical waveform extends to a large number of orbits, which can be computationally prohibitive; otherwise, only for binary masses $\gtrsim 100 M_\odot$ is the splicing error negligible.

TABLE V. Error norms of the (2, 2) spherical harmonic mode for the Bondi news N, its counterpart N_Ψ (obtained by time integral of the Weyl component Ψ) and for the differences $N_{\Delta R}$ comparing extraction at radii $R_E = 20M$ and $R_E = 50M$ to extraction at $R_E = 100M$.

Variable	Re	Im
$\mathcal{E}_1(N)_{R=20}$	8.76×10^{-4}	8.74×10^{-4}
$\mathcal{E}_1(N)_{R=50}$	2.62×10^{-4}	2.60×10^{-4}
$\mathcal{E}_1(N)_{R=100}$	1.21×10^{-4}	1.22×10^{-4}
$\mathcal{E}_1(N_\Psi)_{R=20}$	1.08×10^{-3}	1.12×10^{-3}
$\mathcal{E}_1(N_\Psi)_{R=50}$	3.33×10^{-4}	2.93×10^{-4}
$\mathcal{E}_1(N_\Psi)_{R=100}$	2.30×10^{-4}	1.68×10^{-4}
$\mathcal{E}_1(N_{\Delta R(20,100)})$	5.41×10^{-3}	5.55×10^{-3}
$\mathcal{E}_1(N_{\Delta R(50,100)})$	4.28×10^{-3}	4.51×10^{-3}

An advantage of the $\mathcal{E}_1$ error norm based upon the news function is that the denominator in (7.1) is directly related to the radiated energy. As a result, the factor by which $\mathcal{E}_1(N)$ is overestimated is $\mathcal{F}^{-1/2}$, where

$$\mathcal{F} := \frac{\Delta E(\text{Numerical})}{\Delta E(\text{Chirp}) + \Delta E(\text{Numerical})} \tag{7.10}$$

and ΔE denotes the energy radiated in the indicated time periods. The total energy radiated during the post-Newtonian inspiral and merger can be estimated from the difference between the final black hole mass M_H and the mass M_0 of the binary for a large initial orbit. The energy $\Delta E(\text{Numerical})$ radiated during the numerically modeled time period can be obtained from the Bondi mass-loss formula. For the binary inspiral being considered here, the final black hole mass is $M_H \approx 0.965187$; the initial mass of the system at infinite separation (given by the sum of the individual black hole masses) is $M_0 \approx 1.01447$; and $\Delta E(\text{Numerical}) \approx 0.0346$. This leads to the fraction of energy $\mathcal{F} \approx .702$ radiated during the numerical period, or

$$\mathcal{F}^{-1/2} \approx 1.19 \tag{7.11}$$

for the factor by which the $\mathcal{E}_1$ errors in Table V are overestimated. We reemphasize that the values in the Table do not include the error introduced by splicing the post-Newtonian and numerical waveforms.

Besides the values $\mathcal{E}_1(N)$ of the numerical truncation error in the real and imaginary part of the news function extracted at $R_E = 20M$, $50M$ and $100M$, Table V includes the corresponding truncation error $\mathcal{E}_1(N_\Psi)$ obtained from integrating Ψ via (3.4). The Table also includes the modeling errors $\mathcal{E}_1(N_{\Delta R(20,100)})$ and $\mathcal{E}_1(N_{\Delta R(50,100)})$ in the news which results from the differences $N_{R=20} - N_{R=100}$ and $N_{R=50} - N_{R=100}$ obtained from extracting the waveform at radii $R_E = 50M$ and $R_E = 20M$ compared with extraction at $R_E = 100M$. In computing these error norms, we integrate over the interval corresponding to $t/M \geq 100$ in Fig. 13 to eliminate effects of the initial junk radiation.

Consider first the criterion for detection where we set $\epsilon_{\max} = .005$, which for advanced LIGO ensures less than a 10% signal loss, a target which is often adopted in LIGO searches for compact binaries [37]. For this target, (7.5) reduces to $\mathcal{E}_1 \leq 0.1 C_1$, or $\mathcal{E}_1 \leq .024$ for the low mass bound $C_1 \approx .24$. This criterion is easily satisfied by all the error norms in Table V. Thus the advanced LIGO detection criterion is satisfied by CCE waveforms obtained from either the news or Weyl component throughout the entire binary mass range. In addition, the detection criterion is unaffected by modeling errors introduced by choice of extraction radius. Note that the $\mathcal{E}_1(N)$ and $\mathcal{E}_1(N_\Psi)$ errors decrease with larger extraction radius. This is expected since the truncation error introduced by the characteristic evolution code depends upon the size of the integration region between the extraction worldtube and $\mathcal{I}^+$.

The criterion for measurement is more stringent. For a calibration factor given by the expected lower bound $\eta_{\min} = 0.4$ and for the lower bound $C_1 \approx .24$ corresponding to the small mass limit, (7.9) reduces to

$$\mathcal{E}_1 \leq C_1 \frac{\eta_c}{\rho} = \frac{9.6 \times 10^{-2}}{\rho}. \tag{7.12}$$

For the most optimistic advanced LIGO signal-to-noise ratio, which is expected to be $\rho \approx 100$ for the strongest and best tuned events, the requirement for measurement is then $\mathcal{E}_1 \leq 9.6 \times 10^{-4}$. Thus, comparing (7.12) to the values in Table V, the advanced LIGO measurement criterion is satisfied throughout the entire binary mass range by the numerical truncation error $\mathcal{E}_1(N)$ in the CCE waveform obtained from the news function. The $\mathcal{E}_1(N_\Psi)$ error obtained from the Weyl component for extraction radii $R_E \geq 50M$ also satisfy this full range of measurement standards. The value of $\mathcal{E}_1(N_\Psi)$ for $R_E = 20M$ would satisfy the full range of measurement standards for $\rho < 100$ if reduced by the factor $\mathcal{F}^{-1/2}$ given in (7.11). Note also that the truncation error is being conservatively measured by the $O(\Delta^2)$ error (6.3), rather than the third order accurate error in the Richardson extrapolated waveform.

These results can be compared with the measurement criterion for advanced LIGO data analysis reported in the Samurai project [55], which was also based upon a nonspinning, equal-mass binary black hole inspiral and merger. There it was found that the mismatch between perturbative waveforms obtained using various Cauchy codes limited the measurement application to signal-to-noise ratios $\rho \lesssim 25$. This is consistent with our experience, and that reported in [9], that the additional truncation error introduced by applying CCE to a Cauchy simulation of a binary inspiral is much smaller than the numerical error resulting from the Cauchy code.

The values of $\mathcal{E}_1(N_{\Delta R})$ in Table V give an estimate of the modeling error introduced by different choices of extraction radius. The error $\mathcal{E}_1(N_{\Delta R(50,100)})$, introduced by extraction at $R_E = 50M$ as compared to $R_E = 100M$, only satisfies the full range of measurement standards for signal-to-noise ratios $\rho < 21$, or $\rho < 25$ if (7.11) is taken into account. This would cover the most likely advanced LIGO events. These modeling errors primarily result from initialization effects which we have discussed and which would be less significant in simulations with a higher number of orbits. The results suggest that the choice of extraction radius should be balanced between a sufficiently large radius to reduce initialization effects and a sufficiently small radius where the Cauchy grid is more highly refined and outer boundary effects are better isolated. For the Cauchy grid setup in the present case, there is a factor of 2 in refinement at $r = 50M$ compared to $r = 100M$, which for 8th order finite differencing has considerable impact on the error. Future experiments with longer runs involving more orbits will supply valuable guidance for optimizing the extraction radius.

Table VI gives some pertinent $\mathcal{E}_2$ error norms for the (2, 2) spherical harmonic component. Besides the numerical truncation error $\mathcal{E}_2(\Psi)$ obtained for characteristic extraction at $R_E = 20M$, $R_E = 50M$ and $R_E = 100M$, the table includes the error norm $\mathcal{E}_2(\delta\psi)$ measuring the difference between perturbative and characteristic extraction, as defined in (7.4), obtained at $R_E = 50M$ and $R_E = 100M$. The table also includes the modeling error $\mathcal{E}_2(\Psi_{\Delta R(50,100)})$ resulting from the difference $\Psi_{R=50} - \Psi_{R=100}$ obtained using characteristic extraction at radii $R_E = 50M$ and $R_E = 100M$, as well as the corresponding error norm $\mathcal{E}_2(\psi_{4,\Delta R(50,100)})$ resulting from the difference obtained using perturbative extraction at $R_E = 50M$ and $R_E = 100M$, i.e.

$$\mathcal{E}_2(\mathrm{Re}\psi_{4,\Delta R(50,100)}) = \frac{\|\mathrm{Re}[(r\psi_4/2)|_{r=100M} - (r\psi_4/2)|_{r=50M}]\|}{\|\mathrm{Re}\Psi\|} \tag{7.13}$$

TABLE VI. $\mathcal{E}_2$ error norms for the (2, 2) spherical harmonic mode of the CCE waveform Ψ obtained using extraction worldtube radii $R_E = 20M$, $R_E = 50M$ and $R_E = 100M$ and the norms of the difference $\delta\psi$ between Ψ and the perturbative ψ_4 waveforms extracted at $50M$ and $100M$. We also tabulate the modeling error $\mathcal{E}_2(\Psi_{\Delta R(50,100)})$ resulting from the difference in extracting Ψ at $50M$ and $100M$, and the corresponding modeling error $\mathcal{E}_2(\psi_{4,\Delta R(50,100)})$ for extraction via ψ_4.

Variable	Re	Im
$\mathcal{E}_2(\Psi)_{R=20}$	1.14×10^{-3}	1.17×10^{-3}
$\mathcal{E}_2(\Psi)_{R=50}$	4.04×10^{-4}	3.53×10^{-4}
$\mathcal{E}_2(\Psi)_{R=100}$	2.81×10^{-4}	2.09×10^{-4}
$\mathcal{E}_2(\delta\psi)_{R=50}$	5.09×10^{-3}	5.08×10^{-3}
$\mathcal{E}_2(\delta\psi)_{R=100}$	6.81×10^{-3}	6.32×10^{-3}
$\mathcal{E}_2(\Psi_{\Delta R(50,100)})$	1.94×10^{-2}	1.91×10^{-2}
$\mathcal{E}_2(\psi_{4,\Delta R(50,100)})$	3.13×10^{-2}	3.14×10^{-2}

$$\mathcal{E}_2(\mathrm{Im}\,\psi_{4,\Delta R(50,100)}) = \frac{\|\mathrm{Im}[(r\psi_4/2)|_{r=100M} - (r\psi_4/2)|_{r=50M}]\|}{\|\mathrm{Im}\Psi\|}. \quad (7.14)$$

All norms are again computed over the time interval $t/M \geq 100$ indicated in Fig. 13 to reduce effects of initial junk radiation.

Although the $\mathcal{E}_2$ norms are not effective for low mass binaries, they give some useful information for comparing extraction at various radii and comparing characteristic and perturbative extraction. In the high mass limit for which $C_2 = 1$ and with the same lower limits for $\epsilon_{\max}$ and η_c as for the $\mathcal{E}_1$ norms, the detection criterion (7.5) reduces to

$$\mathcal{E}_2 \leq \sqrt{2\epsilon_{\max}} = 0.1 \quad (7.15)$$

and the measurement criterion (7.6) reduces to

$$\mathcal{E}_2 \leq \frac{\eta_c}{\rho} = \frac{0.4}{\rho}. \quad (7.16)$$

All the error norms in Table VI satisfy the detection requirement for this high mass limit. The truncation errors $\mathcal{E}_2(\Psi)$ decrease with extraction radius as in the case of the $\mathcal{E}_1(N_\Psi)$ errors. The values at all three extraction radii satisfy the measurement requirement for the most optimistic advanced LIGO signal-to-noise ratio $\rho = 100$. These results are consistent with the $\mathcal{E}_1(N_\Psi)$ error in Table V obtained by integrating Ψ.

The norms $\mathcal{E}_2(\delta\psi)$ measure the difference between characteristic and perturbative extraction. The results in the Table show that this difference is fairly independent of whether the waveforms are extracted at $R_E = 50M$ or $R_E = 100M$. In the high mass limit in which (7.16) is valid, these errors impact the measurement criterion only for signal-to-noise ratios $\rho > 59$ but they could be expected to be more significant for low mass binaries. Whether the $\mathcal{E}_2(\delta\psi)$ error can be attributed to characteristic extraction or to perturbative extraction cannot be decided from this single test and deserves further investigation. A definitive answer would of course require knowledge of the "exact" waveform.

The modeling error $\mathcal{E}_2(\psi_{4,\Delta R(50,100)})$, which results from comparing perturbative extraction at $R_E = 50M$ and $R_E = 100M$, is considerably larger than the corresponding modeling error $\mathcal{E}_2(\Psi_{\Delta R(50,100)})$ for characteristic extraction. This confirms the expectation that perturbative extraction requires a large extraction radius. Both of these modeling errors are substantial, which further emphasizes the importance of an optimal choice of extraction radius.

VIII. CONCLUSION

We have developed a new characteristic waveform extraction tool. Bugs and inconsistencies in the previous version have been eliminated. The extracted waveform from a binary black hole inspiral now shows clean convergence. We have demonstrated that this allows the use of Richardson extrapolation to obtain third order accurate waveforms whose numerical truncation error satisfies the advanced LIGO standards for detection and measurement. Characteristic waveform extraction from a binary black hole inspiral can now be obtained without any recourse to linearization and from extraction radii as small as $R = 20M$. The Cauchy interface has been simplified in terms of a spectral decomposition.

There are still elements where accuracy could be improved. Some of these, such as more accurate start-up algorithms for the radial integrations at the extraction worldtube and more accurate asymptotic limits at $\mathcal{I}^+$, might be handled by small modifications but others, such as extending the overall accuracy to 4th or higher order, would entail a more major overhaul of the underlying PITT code. This is perhaps long overdue, but a proper treatment would require a better understanding of the underlying mathematical problem. The well-posedness of the gravitational worldtube-nullcone initial-boundary value problem upon which the code is based has not yet been established. Only recently has well-posedness been demonstrated for the corresponding nonlinear scalar wave problem [60]. The PITT code was developed in the early days of numerical relativity when considerations of well-posedness did not arise in the formulation of Cauchy as well as characteristic codes. The development of a stable characteristic code involved "educated guesses". Today, the numerical relativity community is more aware of the benefits that a well-posed problem can bring. Most important, a proof of well-posedness of the continuum problem by means of energy estimates can be converted to ensure stability of the corresponding finite-difference problem by the analogous estimates obtained by summation by parts. A new characteristic code based upon this approach would be of great value. Of equal value would be the implementation of Cauchy-characteristic matching (CCM), in which the characteristic evolution is used to supply outer boundary data for the Cauchy evolution. So far, CCM has only been successfully applied to a harmonic Cauchy code in the linearized regime [61].

Although there is room for further improvement in the CCE tool presented here, there also is pressing interest from several numerical relativity groups to apply the tool to extract waveforms from binary black hole inspirals. The emerging importance of this problem to the future of gravitational wave astronomy has created an urgency to make characteristic waveform extraction widely available. Simulations of binary black hole inspirals are too computationally expensive to be carried out solely for the purpose of wave extraction tests. This would conflict with the demands to apply computational resources to results of importance to gravitational wave astronomy and binary black hole astrophysics. However, the extra computational expense of adding characteristic extraction to a Cauchy

simulation is fractionally small. For our tests, where we extracted twice as often as required, the interpolation, decomposition, and saving of the metric data used only $\approx 6.9\%$ of the total simulation time. The application of characteristic extraction to simulations of astrophysical importance will at the same time provide a practical approach to improving the extraction tool by comparing results obtained with different formulations, different numerical techniques and different grid specifications. In particular, our test results emphasize the need for a better understanding of the optimal choice of extraction radius, which would balance between the discretization error in the Cauchy code, the initialization error, the error originating at the outer Cauchy boundary and the relatively small discretization error from CCE.

We have demonstrated here how the module can be applied to the LazEv code, which is a finite-difference BSSN code, to produce calibrated binary black hole waveforms. We welcome applications to codes based upon other formulations of the Einstein equations, e.g. the harmonic formulation, and based upon other numerical methods, e.g. spectral methods. In particular, characteristic extraction offers a way to unambiguously compare binary black hole waveforms obtained from the same initial data using codes based upon different formulations of the Einstein equations, different numerical techniques, different evolution gauges and different methods of treating the internal singularities (by punctures or by excision). Such comparisons would be of especial importance in the case of precessing binaries composed of high spin black holes, where the reliability of perturbative extraction has not been extensively tested.

We have made the present characteristic waveform extraction tool publicly available as part of the Einstein Toolkit [62].

ACKNOWLEDGMENTS

We thank L. Lindblom and C. Reisswig for many helpful discussions. B. S. acknowledges support from the Sherman Fairchild Foundation and NSF grants PHY-061459 and PHY-0652995 to the California Institute of Technology. J. W. acknowledges support from NSF grants PHY-0553597 and PHY-0854623 to the University of Pittsburgh. Y. Z. acknowledges support from NSF grants PHY-0722315, PHY-0653303, PHY-0714388, PHY-0722703, DMS-0820923, PHY-0929114, PHY-0969855, and NSFCDI-1028087 and NASA grants 07-ATFP07-0158 and HST-AR-11763 to RIT and computational resources provided by the Ranger cluster at TACC (Teragrid allocations TG-PHY080040N and TG-PHY060027N) and by NewHorizons at RIT. M. C. B. acknowledges support from NSF grant PHY-0969709 to the Marshall University and computational resources provided by the Teragrid allocation TG-PHY090008. M. C. B. and B. S. thank the University of Pittsburgh for hospitality during the major part of this project. An essential component of this work is the PITT null code, to which N. T. Bishop, R. Gómez, R. A. Isaacson, L. Lehner, P. Papadopoulos, and J. Welling have made major contributions.

APPENDIX: CODE REVISION

Revisions to the worldtube module:

(i) The numerical error in the previous version of the worldtube module did not converge properly upon grid refinement. We have traced this problem to an inconsistency in the start-up algorithm for the integration of the characteristic equations away from the extraction worldtube. Data from the Cauchy code had been used in an overdetermined manner to supply the integration constants for the characteristic equations. As a result, the Cauchy evolution introduced inconsistencies with the characteristic equations which degraded convergence of the numerical error. We have revamped this start-up algorithm so that the worldtube module now has clean second order accuracy with respect to grid size.

(ii) We have found and corrected bugs which had been introduced in the implementation of features designed to improve code performance. In particular, in parallelizing the code using the Cactus framework [50], a complex spin-weighted term in the evolution module was incorrectly declared to be a real variable. In addition, it had been suggested that improved accuracy could be obtained by reducing second derivatives in the angular directions to first order form by the use of auxiliary variables [41]. In the process of doing so, values of certain variables in the subroutines for the data at the extraction worldtube were inadvertently interchanged between the North and South stereographic patches. The introduction of these bugs made the resulting code inconsistent with the Einstein equations. (From tracing through the code archive, we determined that the bugs were introduced in 2002 or later so that they do not affect the validity of results prior to 2002. C. Reisswig has informed us that he recomputed some of the results in [8,9] using the corrected code and found good qualitative agreement with the original results.)

(iii) The matching interface has been simplified by introducing a pseudospectral decomposition of the Cauchy metric in the neighborhood of the extraction worldtube. This provides more economical storage of the inner boundary data for the characteristic code so that the waveform at $\mathcal{I}^+$ can be obtained with small computational burden compared to the Cauchy evolution.

(iv) Interpolation error arises because the characteristic grid points do not lie exactly on the extraction worldtube determined by the Cauchy coordinates.

The interpolation stencils change in a discontinuous way when the grid is refined. Consequently, although this interpolation error is second order in grid size, there is a small stochastic component relative to the choice of grid. This can obscure the results of convergence tests. We have reduced such sources of error so that convergence tests can be used to validate the interface modules.

(v) We have streamlined the start-up procedure at the extraction worldtube by initializing the auxiliary variables (introduced to remove second angular derivatives) directly in terms of the main variables.

(vi) In previous applications of the extraction module, it was expedient to set the characteristic data on the initial hypersurface to zero outside some radius. This necessitated a transition region to obtain continuity with the initial Cauchy data, which requires nonzero initial characteristic data at the extraction worldtube. Here we initialize the data by requiring that the Newman-Penrose component of the Weyl tensor intrinsic to the initial null hypersurface vanish, i.e. $\psi_0 = 0$. For a linear perturbation of the Schwarzschild metric, this condition eliminates incoming radiation crossing the initial null hypersurface. Since ψ_0 consists of a second radial derivative of the characteristic data, this condition allows both continuity at the extraction worldtube and the desired asymptotic falloff of the characteristic data at infinity.

Modifications of the PITT code:

(i) A source of error in characteristic evolution is the intergrid interpolations arising from the stereographic patches used to coordinatize the spherical cross-sections of the outgoing null hypersurfaces. The previous version of the code used two square stereographic patches centered about the North and South poles, each overlapping the equator. This has now been modified by shrinking the overlap region so that each patch has a circular boundary located slightly past the equator, as is the practice in the use of stereographic grids in meteorology [63]. This eliminates the region near the corners of the square patch where the numerical error was most troublesome. Angular numerical dissipation has also been introduced and shown to be effective in controlling the short wavelength noise arising from the intergrid interpolations across the stereographic patches. Tests show that the resulting waveforms have smooth numerical error as functions on the sphere [5].

Characteristic codes based upon a six patch covering of the sphere [64,65] offer the potential for better accuracy but they have not yet been developed to handle waveform extraction. See [5] for a comparison of the six patch and the stereographic approaches on a test problem.

(ii) The accuracy of the angular derivatives has been increased to a fourth-order finite-difference approximation, as opposed to the second-order accuracy in the original code. The radial derivatives and time integration remain second order accurate.

(iii) Some of the differential equations governing propagation along the characteristics become degenerate at $\mathcal{I}^+$ and affect the accuracy of asymptotic quantities such as the Bondi news function. The correct asymptotic behavior has now been incorporated into the finite-difference approximation in order to increase accuracy. In addition, the accuracy of certain one-sided finite-difference approximations necessary at $\mathcal{I}^+$ has also been improved.

(iv) In addition, the code has been extended to supply the waveform at $\mathcal{I}^+$ in terms of the radiative component of the Weyl tensor as well as the Bondi news function. For tests in the linearized regime, extraction via the Weyl tensor was found to be slightly more accurate than via the news function when large gauge effects are introduced in the characteristic coordinates [5]. On the other hand, the higher derivatives involved in computing the Weyl tensor lead to less smoothness in the numerical error. Overall, the two methods are competitive.

[1] , J. G. Baker, and B. J. Owen, Phys. Rev. D **82**, 084020 (2010).

[2] B. Abbott *et al.* (LIGO Scientific Collaboration), Rep. Prog. Phys. **72**, 076901 (2009).

[3] F. Acernese *et al.* (Virgo Collaboration), Classical Quantum Gravity **25**, 114045 (2008).

[4] L. Lehner and O. M. Moreschi, Phys. Rev. D **76**, 124040 (2007).

[5] M. C. Babiuc, N. T. Bishop, B. Szilágyi, and J. Winicour, Phys. Rev. D **79**, 084011 (2009).

[6] N. T. Bishop, R. Gómez, L. Lehner, B. Szilágyi, J. Winicour, and R. A. Isaacson, in *Black Holes, Gravitational Radiation and the Universe*, edited by B. Iyer and B. Bhawal (Kluwer Academic Publishers, Dordrecht, 1998).

[7] N. T. Bishop, R. Gómez, L. Lehner, and J. Winicour, Phys. Rev. D **54**, 6153 (1996).

[8] C. Reisswig, N. T. Bishop, D. Pollney, and B. Szilágyi, Phys. Rev. Lett. **103**, 221101 (2009).

[9] C. Reisswig, N. T. Bishop, D. Pollney, and B. Szilágyi, Classical Quantum Gravity **27**, 075014 (2010).

[10] C. Reisswig, C. D. Ott, U. Sperhake, and E. Schnetter, Phys. Rev. D **83**, 064008 (2011).
[11] C. Reisswig and D. Pollney, arXiv:1004.4209.
[12] S. Hahn and R. W. Lindquist, Ann. Phys. (N.Y.) **29**, 304 (1964).
[13] L. Smarr, A. Cadez, B. de Witt, and K. R. Eppley, Phys. Rev. D **14**, 2443 (1976).
[14] R. Matzner, H. E. Seidel, S. L. Shapiro, L. Smarr, W.-M. Suen, S. A. Teukolsky, and J. Winicour (The Binary Black Hole Grand Challenge Alliance), Science **270**, 941 (1995).
[15] R. Arnowitt, S. Deser, and C. W. Misner, *Gravitation: An Introduction to Current Research*, edited by L. Witten (Wiley, New York, 1962).
[16] F. Pretorius, Phys. Rev. Lett. **95**, 121101 (2005).
[17] M. Campanelli, C. O. Lousto, P. Marronetti, and Y. Zlochower, Phys. Rev. Lett. **96**, 111101 (2006).
[18] J. G. Baker, J. Centrella, D.-I. Choi, M. Koppitz, and J. van Meter, Phys. Rev. Lett. **96**, 111102 (2006).
[19] M. Shibata and T. Nakamura, Phys. Rev. D **52**, 5428 (1995).
[20] T. Baumgarte and S. L. Shapiro, Phys. Rev. D **59**, 024007 (1998).
[21] H. Bondi, M. J. G. van der Burg, and A. W. K. Metzner, Proc. R. Soc. A **269**, 21 (1962).
[22] R. K. Sachs, Proc. R. Soc. A **270**, 103 (1962).
[23] R. Penrose, Phys. Rev. Lett. **10**, 66 (1963).
[24] L. A. Tamburino and J. Winicour, Phys. Rev. **150**, 1039 (1966).
[25] R. A. Isaacson, J. S. Welling, and J. Winicour, J. Math. Phys. (N.Y.) **24**, 1824 (1983).
[26] N. T. Bishop, R. Gómez, L. Lehner, M. Maharaj, and J. Winicour, Phys. Rev. D **56**, 6298 (1997).
[27] M. Babiuc, B. Szilágyi, I. Hawke, and Y. Zlochower, Classical Quantum Gravity **22**, 5089 (2005).
[28] R. Gómez *et al.* (The Binary Black Hole Grand Challenge Alliance), Phys. Rev. Lett. **80**, 3915 (1998).
[29] R. Gómez, L. Lehner, L. R. L. Marsa, and J. Winicour, Phys. Rev. D **57**, 4778 (1998).
[30] R. Gómez, S. Husa, L. Lehner, and J. Winicour, Phys. Rev. D **66**, 064019 (2002).
[31] Y. Zlochower, R. Gómez, S. Husa, L. Lehner, and J. Winicour, Phys. Rev. D **68**, 084014 (2003).
[32] J. Winicour, Living Rev. Relativity **12**, 3 (2009).
[33] F. Siebel, J. A. Font, E. Müller, and P. Papadopoulos, Phys. Rev. D **67**, 124018 (2003).
[34] F. Linke, J. A. Font, H. T. Janka, E. Müller, and P. Papadopoulos, Astron. Astrophys. **376**, 568 (2001).
[35] N. T. Bishop, R. Gómez, S. Husa, L. Lehner, and J. Winicour, Phys. Rev. D **68**, 084015 (2003).
[36] É. É. Flanagan and S. A. Hughes, Phys. Rev. D **57**, 4535 (1998).
[37] L. Lindblom, B. J. Owen, and D. A. Brown, Phys. Rev. D **78**, 124020 (2008).
[38] L. Lindblom, Phys. Rev. D **80**, 042005 (2009).
[39] E. T. Newman and R. Penrose, J. Math. Phys. (N.Y.) **7**, 863 (1966).
[40] R. Gómez, L. Lehner, P. Papadopoulos, and J. Winicour, Classical Quantum Gravity **14**, 977 (1997).
[41] R. Gómez, Phys. Rev. D **64**, 1 (2001).
[42] L. Lehner, J. Comput. Phys. **149**, 59 (1999).
[43] E. T. Newman and R. Penrose, J. Math. Phys. (N.Y.) **3**, 566 (1962).
[44] J. Winicour, Gen. Relativ. Gravit. **19**, 281 (1987).
[45] N. T. Bishop, Classical Quantum Gravity **22**, 2393 (2005).
[46] R. K. Sachs, J. Math. Phys. (N.Y.) **3**, 908 (1962).
[47] R. Gómez and J. Winicour, J. Math. Phys. (N.Y.) **33**, 1445 (1992).
[48] M. Campanelli, C. O. P. Marronetti, and Y. Zlochower, Phys. Rev. Lett. **96**, 111101 (2006).
[49] Y. Zlochower, J. G. Baker, M. Campanelli, and C. O. Lousto, Phys. Rev. D **72**, 024021 (2005).
[50] See Cactus Computational Toolkit home page at http://www.cactuscode.org.
[51] E. Schnetter, S. H. Hawley, and I. Hawke, Classical Quantum Gravity **21**, 1465 (2004).
[52] J. G. Baker, J. Centrella, D.-I. Choi, M. Koppitz, and J. van Meter, Phys. Rev. Lett. **96**, 111102 (2006).
[53] M. Campanelli, C. O. Lousto, and Y. Zlochower, Phys. Rev. D **74**, 041501 (2006).
[54] C. O. Lousto, H. Nakano, Y. Zlochower, and M. Campanelli, Phys. Rev. D **82**, 104057 (2010).
[55] M. Hannam, S. Husa, J. G. Baker, M. Boyle, B. Brügmann, T. Chu, N. Dorband, F. Hermann, I. Hinder, B. J. Kelly, L. E. Kidder, P. Laguna, K. D. Matthews, J. R. van Meter, H. P. Pfeiffer, D. Pollney, C. Reisswig, M. A. Scheel, and D. Shoemaker, Phys. Rev. D **79**, 084025 (2009).
[56] M. Boyle, D. A. Brown, L. E. Kidder, A. H. Mroue, H. P. Pfeiffer, M. A. Scheel, G. B. Cook, and S. A. Teukolsky, Phys. Rev. D **76**, 124038 (2007).
[57] L. Lindblom, Phys. Rev. D **80**, 064019 (2009).
[58] M. Hannam, S. Husa, F. Ohme, and P. Ajith, Phys. Rev. D **82**, 124052 (2010).
[59] H. MacDonald, S. Nissake, and H. P. Pfeiffer, Classical Quantum Gravity **28**, 134002 (2011).
[60] H.-O. Kreiss and J. Winicour, Classical Quantum Gravity **28**, 145020 (2011).
[61] B. Szilágyi and J. Winicour, Phys. Rev. D **68**, 1 (2003).
[62] See Einstein Toolkit Consortium home page at http://www.einsteintoolkit.org.
[63] G. L. Browning, J. J. Hack, and P. N. Swarztrauber, Mon. Weather Rev. **117**, 1058 (1989).
[64] C. Reisswig, N. T. Bishop, C. W. Lai, J. Thornburg, and B. Szilágyi, Classical Quantum Gravity **24**, S327 (2007).
[65] R. Gómez, W. Barreto, and S. Frittelli, Phys. Rev. D **76**, 124029 (2007).